OPEN ACCESS Freely available online

PLOS ONE

High Temperature Stability of Onion-Like Carbon vs Highly Oriented Pyrolytic Graphite

Alessandro Latini[1], Massimo Tomellini[2], Laura Lazzarini[3], Giovanni Bertoni[3], Delia Gazzoli[1], Luigi Bossa[1], Daniele Gozzi[1]*

1 Dipartimento di Chimica, Università di Roma La Sapienza, Roma, Italy, **2** Dipartimento di Scienze e Tecnologie Chimiche, Università di Roma Tor Vergata, Roma, Italy, **3** IMEM – CNR, Parma, Italy

Abstract

The thermodynamic stability of onion-like carbon (OLC) nanostructures with respect to highly oriented pyrolytic graphite (HOPG) was determined in the interval 765–1030 K by the electromotive force (*emf*) measurements of solid electrolyte galvanic cell: (Low) Pt|Cr_3C_2,CrF_2,OLC|CaF_2s.c.|Cr_3C_2,CrF_2,HOPG|Pt (High). The free energy change of transformation HOPG = OLC was found positive below 920.6 K crossing the zero value at this temperature. Its trend with temperature was well described by a 3rd degree polynomial. The unexpected too high values of $\left(\frac{\partial \Delta_r H_T}{\partial T}\right)_P = \Delta c_P(T)$ jointly to the HR-TEM, STEM and EELS evidences that showed OLC completely embedded in rigid cages made of a Cr_3C_2/CrF_2 matrix, suggested that carbon in the electrodes experienced different internal pressures. This was confirmed by the evaluation under constant volume of $\frac{dP}{dT}$ by the $\frac{\alpha}{\kappa}$ ratio for OLC (0.5 MPa K^{-1}) and HOPG (8 Pa K^{-1}) where α and κ are the isobaric thermal expansion and isothermal compressibility coefficients, respectively. The temperature dependency of the pressure was derived and utilized to calculate the enthalpy and entropy changes as function of temperature and pressure. The highest value of the internal pressure experienced by OLC was calculated to be about 7 GPa at the highest temperature. At 920.6 K, $\Delta_r H$ and $\Delta_r S$ values are 95.8 kJ mol^{-1} and 104.1 JK^{-1} mol^{-1}, respectively. The surface contributions to the energetic of the system were evaluated and they were found negligible compared with the bulk terms. As a consequence of the high internal pressure, the values of the enthalpy and entropy changes were mainly attributed to the formation of carbon defects in OLC considered as multishell fullerenes. The change of the carbon defect fraction is reported as a function of temperature.

Citation: Latini A, Tomellini M, Lazzarini L, Bertoni G, Gazzoli D, et al. (2014) High Temperature Stability of Onion-Like Carbon vs Highly Oriented Pyrolytic Graphite. PLoS ONE 9(8): e105788. doi:10.1371/journal.pone.0105788

Editor: Danilo Roccatano, Jacobs University Bremen, Germany

Received March 19, 2014; **Accepted** July 24, 2014; **Published** August 25, 2014

Data Availability: The authors confirm that all data underlying the findings are fully available without restriction. All relevant data are within the paper and its Supporting Information files.

Funding: This work was partially financed through the PRIN 2009 Project no. 2009N4BJ4J and "Acquisizione di medie e grandi attrezzature scientifiche 2010" Università di Roma La Sapienza, no. C26G10KKK5. The funders had no role in study design, data collection and analysis, decision to publish, or preparation of the manuscript.

Competing Interests: The authors have declared that no competing interests exist.

* Email: daniele.gozzi@uniroma1.it

Introduction

The modifications of the internal arrangements and related energies of single wall carbon nanotubes (SWCNTs) in bundles were studied [1] by our group in the particular situation where their dilatation due to the high temperatures was hindered being the bundles embedded in a matrix much less dilatable. This generates high internal pressures, which are a direct consequence of the increase of the internal energy of the system producing changes in the SWCNT configuration inside the bundle and deformation of SWCNTs too.

The knowledge of the thermodynamic stability of nanostructures is a fundamental aspect to design new nanostructured materials as well as to forecast their behaviour. Most of the information on this subject comes from computational studies [2][3][4][5][6] and to a lesser extent by experimental works [7][8][9]. To the best of author knowledge and with the exception of reference [10][11][12] there are no articles dealing with thermodynamic measurements at high temperature on carbon nanostructures.

On the other hand, the 3D carbon phase diagram, where the third axis is the particle size, is still under consideration. The contribution of the surface energy to the bulk Gibbs free energy per atom of a cluster of n atoms in a given phase is strongly affected by the number of atoms itself. In general, a review of the literature regarding the structure of carbon nanoparticles [13] highlights that at sizes below 1.8 nm, other carbon forms are abundant, such as fullerenes and onion-like carbon (OLC). Therefore, Kuznetsov et al. [14] suggested to assign a corresponding region of the phase diagram to closed-shell sp^2-bonded nanocarbons. In their phase diagram the regions of stability are specifically indicated for fullerenes and OLC for $n = 10$ to 10^2 atoms. The complete and thorough vision of the phase diagrams of these nanostructures in comparison with the phase diagram of the corresponding bulk materials has not been realized yet. There is still a great deal of work to be done in the construction of a

complete *P–T–n* phase diagram of carbon. It is likely however that knowledge gained from theoretical and computational studies [15] of nanocarbon stability plays an important role in the conception of such a diagram, with thermodynamic treatments of phase equilibrium showing the right way for pursuing the final goal.

Onion-like carbon are another class of carbon nanostructures, which are not exhaustively investigated yet though some published results envisage interesting applications such as an easy route to produce diamond nanoparticles [7][8][16] as well as to use them as reaction cells on the nanoscale [9].

The scope of this work is to study, in conditions of reversibility, the thermodynamics of the high temperature transformation under volume constraint from highly oriented pyrolytic graphite (HOPG) to OLC.

Experimental

Since the experimental set-up was published elsewhere [10][11][12] and there is the will of the authors to give in this paper more room to the chemical thermodynamics of our experiment and discussion of the results, we decided to describe more in details the wide experimental part in the Supporting Information S1. A list of all the aspects that took part to the whole experimentation of this work, which are reported in the Supporting Information S1, follows:

1. Starting materials for the electrode preparation
   - 1.1. HOPG, OLC, Cr_3C_2, CrF_2
   - 1.2. Characterization
     - 1.2.1. Thermogravimetry (TG) and Differential Thermal Analysis (DTA)
     - 1.2.2. x-ray diffraction (XRD)
     - 1.2.3. microRaman (mR)
     - 1.2.4. High Resolution Transmission Electron Spectroscopy (HR-TEM)
     - 1.2.5. Electron Energy Loss Spectroscopy (EELS)
     - 1.2.6. X-ray Photoelectron Spectroscopy (XPS)
   - 1.3. Preparation of electrodes and cell assembly
     - 1.3.1. Electrodes
     - 1.3.2. Cell assembly
   - 1.4. Experimental apparatus for the *emf* measurements
   - 1.5. Procedure adopted for the *emf* measurements and their data acquisition
   - 1.6. Analysis of electrodes before and after experiment
     - 1.6.1. X-ray diffraction (XRD)
     - 1.6.2. microRaman spectroscopy (mR)
     - 1.6.3. EELS

Results and Discussion

In order to satisfy the requirement of reversibility, the experimental technique utilized is the electromotive force (*emf*) measurement as function of temperature of galvanic cells, with CaF_2 single crystal as solid electrolyte. Since long time this technique was utilized in our laboratory and it is well known that the method is one of the best way to achieve reliable thermodynamic data.

The galvanic cell:

(Low) Pt|Cr_3C_2,CrF_2,OLC|CaF_2s.c.|Cr_3C_2,CrF_2,HOPG|Pt (High) (A)

was assembled to perform the *emf* vs *T* measurement. Cell A is a fluorine concentration cell being the solid electrolyte an ionic conductor by F^- Frenkel type defects. The positive electrode is the electrode where the chemical potential of F_2(g) is higher and the chemical potential of carbon is lower. This implies that $\Delta\mu_C = -\frac{3}{2}\Delta\mu_{F_2}$. The cell reaction can be written as:

$$\begin{gathered}\frac{3}{2}CrF_2 + C_{HOPG} + 3e = 3F^- + \frac{1}{2}Cr_3C_2 : (+)\\ 3F^- + \frac{1}{2}Cr_3C_2 = 3e + \frac{3}{2}CrF_2 + C_{OLC} : (-)\\ \hline C_{HOPG} = C_{OLC}\end{gathered} \qquad (B)$$

The main advantage of this kind of cells is that no supplementary thermodynamic data are necessary to derive the thermodynamics of the cell reaction. Only the *emf vs T* experimental data are necessary to obtain the reaction Gibbs free energy change, $\Delta_r G$. The reaction changes of enthalpy, $\Delta_r H$, and entropy, $\Delta_r S$, can be also obtained as shown in the followings.

The adopted experimental procedure requires accumulating many isothermal and stationary values of *emf* through several stair shaped thermal cycles each one composed of tens of isotherms. Figure 1 shows the typical behaviour, almost equal for each one, of five tested cells. The first thermal cycles are characterized by hysteresis that tends to disappear. The presence of a vanishing hysteresis in the *emf* trend demonstrates that the whole system of the carbon shells in the OLC and OLC themselves change to reach new stable configurations that convert reciprocally and reversibly as function of temperature. These findings are qualitatively and quantitatively similar to the behaviour we found in the bundles of SWCNTs [1]. The main difference with the present experiment is the final shape of the *emf* vs *T* curve that is characterized here by an exponential growth-like behaviour.

The trend of the Gibbs free energy change is given by:

$$\Delta_r G_T = -3\mathcal{F}E(T) \qquad (1)$$

being 3 the number of moles of electrons exchanged in reaction B and $\mathcal{F}$ the Faraday constant. The curve $E(T)$ is well fit by the 3rd degree polynomial:

$$E(T) = a + bT + cT^2 + dT^3 \qquad (2)$$

.The coefficients and related errors of fit of *emf* vs *T* are given in Table 1. The representation of eq 1 is given in Fig. 2 where at 920.6 K the equality of the chemical potential of carbon $\mu_C(\mathrm{HOPG}) = \mu_C(\mathrm{OLC})$is satisfied.

If each point of the curve of Fig. 2 were a point taken at constant temperature and pressure, the enthalpy change of the transformation, $\Delta_r H_T$, would be given by:

$$\Delta_r H_T = -3\mathcal{F}\left[E(T) - T\left(\frac{\partial E}{\partial T}\right)_P\right] \qquad (3)$$

The temperature dependency of eq 3 should be written as given in any chemical thermodynamics textbook by equation:

$$\left(\frac{\partial \Delta_r H_T}{\partial T}\right)_P = 3\mathcal{F}T\left(\frac{\partial^2 E}{\partial T^2}\right)_P = \Delta c_P(T) \qquad (4)$$

being $\Delta c_P(T) = c_P(\mathrm{OLC}) - c_P(\mathrm{HOPG})$ and c_P the molar heat capacity at constant pressure. In the case of reaction B and at the experimental temperatures, it is expected that $\Delta c_P(T)$ should be

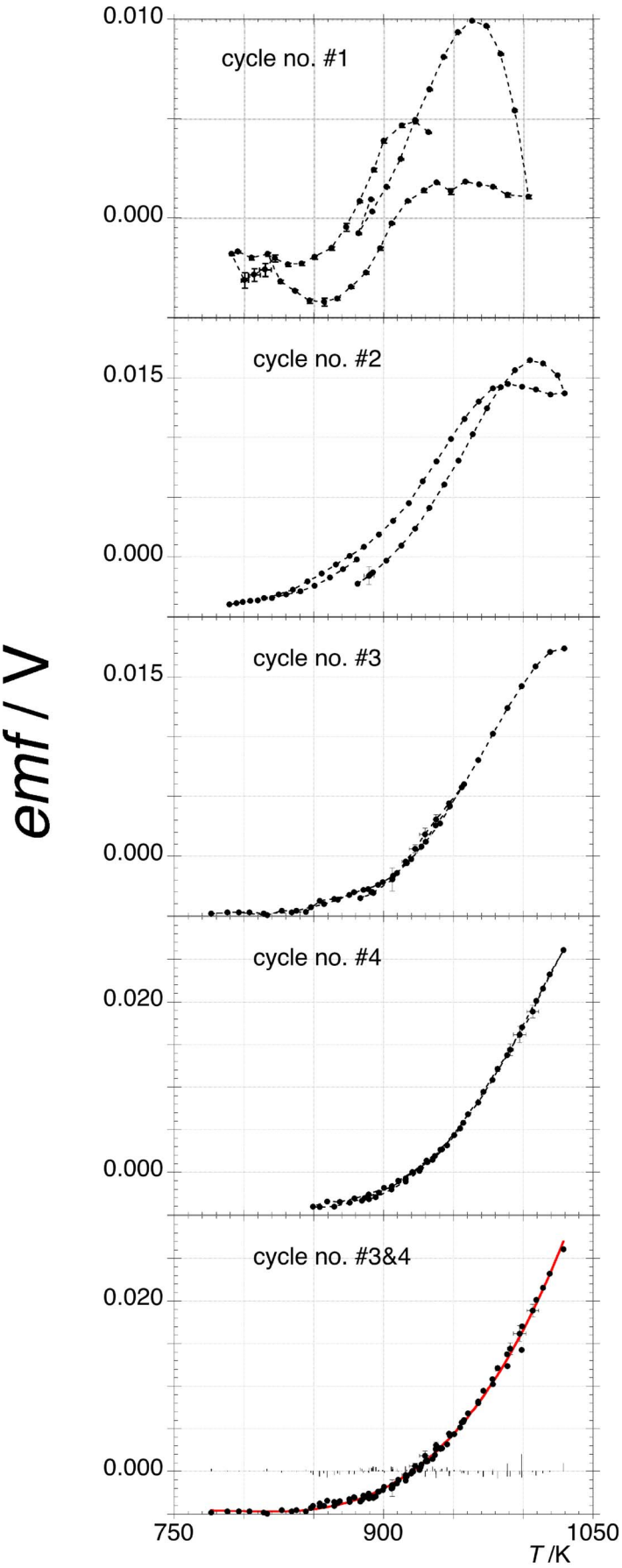
0.010
cycle no. #1
0.000
0.015
cycle no. #2
0.000
0.015
cycle no. #3
0.000
0.020
cycle no. #4
0.000
0.020
cycle no. #3&4
0.000
750
900
1050
T /K
emf / V

Figure 1. The electromotive force (*emf*) vs temperature of galvanic cell A. The progressive disappearing hysteresis is shown from 1st to 3rd thermal cycle (see §1.4 of the Supporting Information S1). The bottom plot combines the 3rd and 4th cycles where the red curve is the best fitting curve given by a 3rd degree polynomial (see Table 1). The residuals of fit are also reported. Most of the error bars are within the size of the experimental points.
doi:10.1371/journal.pone.0105788.g001

quite low. Equation 4 implies the same value of pressure at each temperature for both the electrodes, i.e., $\left(\frac{\partial \Delta_r H_T}{\partial T}\right)_P = \frac{d\Delta_r H_T}{dT}$. The 1st partial derivative against T of eq 3, i.e. eq 4, shows too high $\Delta c_V(T)$ values which are unexpected for the process under study. For this reason, the assumption of constant pressure is not more valid. Therefore, the total derivative of $E(T)$, i.e.,

$$\frac{dE}{dT} = \left(\frac{\partial E}{\partial T}\right)_P + \left(\frac{\partial E}{\partial P}\right)_T \frac{dP}{dT} \tag{5}$$

should be considered where,

$$\left(\frac{\partial E}{\partial P}\right)_T = -\frac{1}{3\mathcal{F}}\left(\frac{\partial \Delta_r G_T}{\partial P}\right)_T = -\frac{1}{3\mathcal{F}}\Delta V \tag{6}$$

being $\Delta V = V(\mathrm{OLC}) - V(\mathrm{HOPG})$ and V is the molar volume. By substituting eq 6 in eq 5 and combining with eq 3, the P, T dependency of $\Delta_r H_T = -3\mathcal{F}\left\{E(T,P) - T\left[\frac{dE}{dT} + \frac{\Delta V}{3\mathcal{F}}\frac{dP}{dT}\right]\right\}$ is found:

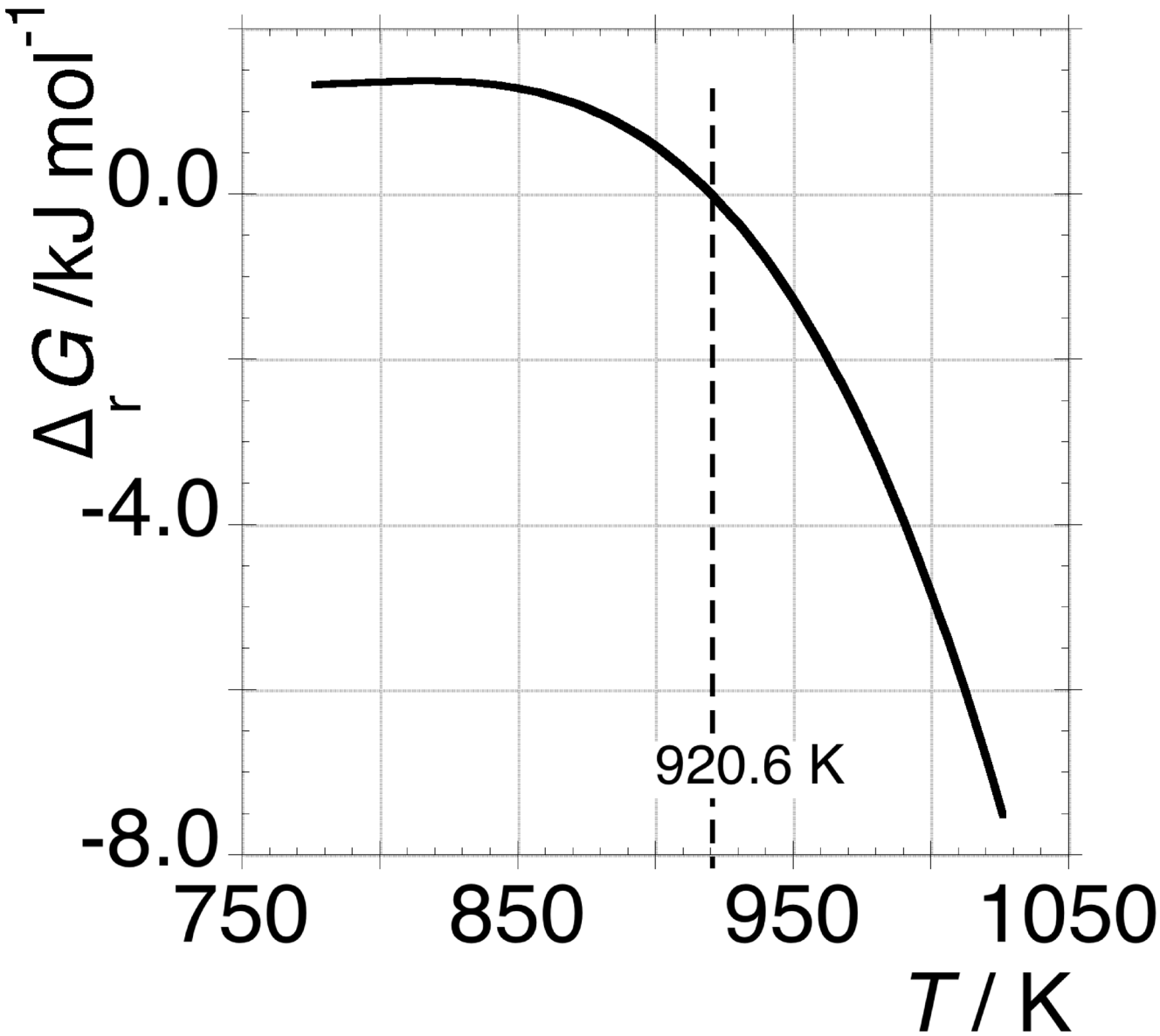

Figure 2. Gibbs free energy change for $C_{HOPG} = C_{OLC}$ transformation calculated according to eq 1. At 920.6 K, the curve crosses zero.
doi:10.1371/journal.pone.0105788.g002

Table 1. Coefficients and related errors of *emf* vs *T* polynomial fit: $E(T)=a+bT+cT^2+dT^3$.

	a/V	*b*/VK^{-1}	*c*/VK^{-2}	*d*/VK^{-3}
coefficient	−1.207	0.0045698	-5.7832×10^{-6}	2.437×10^{-9}
error	0.12433	0.0004144	4.5905×10^{-7}	1.691×10^{-10}

R = 0.99836; $\chi^2 = 1.5935\times10^{-5}$.
doi:10.1371/journal.pone.0105788.t001

$$\Delta_r H_T = -3\mathcal{F}\left\{E(T,P) - T\left[\frac{dE}{dT} + \frac{\Delta V}{3\mathcal{F}}\frac{dP}{dT}\right]\right\} \quad (7)$$

Accordingly, eq 7 differs from eq 3 for the extra term $\left(T\frac{\Delta V}{3\mathcal{F}}\frac{dP}{dT}\right)$, which entails $\frac{dE}{dT} \neq \left(\frac{\partial E}{\partial T}\right)_P$.

The 1st derivative of eq 7 with respect to T is:

$$\frac{d\Delta_r H}{dT} = 3\mathcal{F}T\frac{d^2E}{dT^2} + T\frac{d\Delta V}{dT}\frac{dP}{dT} + \Delta V\frac{dP}{dT} + T\Delta V\frac{d^2P}{dT^2}\ . \quad (8)$$

From the total differential of $\Delta V(T,P)$, the relationship below follows:

$$\frac{d\Delta V}{dT} = \left(\frac{\partial \Delta V}{\partial T}\right)_P + \left(\frac{\partial \Delta V}{\partial P}\right)_T\frac{dP}{dT} = \Delta(\alpha V) - \frac{dP}{dT}\Delta(\kappa V) \quad (9)$$

where α and κ are, respectively, the isobaric volume expansion coefficient and isothermal compressibility. By making use of eq 9, eq 8 can be conveniently modified in the form:

$$\frac{d\Delta_r H}{dT} = 3\mathcal{F}T\frac{d^2E}{dT^2}\left\{T\frac{dP}{dT}\left[\Delta(\alpha V) - \frac{dP}{dT}\Delta(\kappa V)\right]\right\} + \Delta V\frac{dP}{dT} + T\Delta V\frac{d^2P}{dT^2} \quad (10)$$

Equation 10 should be compared with well-known equation [17]:

$$\frac{d\Delta_r H}{dT} = \Delta c_P(T) + [\Delta V - T\Delta(\alpha V)]\frac{dP}{dT} \quad (11)$$

which states that if some phase transition occurs, the equilibrium pressure does not remain constant as the temperature is varied. Since we can write that $\Delta c_P(T) = \Delta c_V(T) + T\Delta\left(\frac{\alpha^2 V}{\kappa}\right)$, by equating eq 10 and eq 11, the following 2nd order differential equation for P is found:

$$\Delta V\frac{d^2P}{dT^2} - \Delta(\kappa V)\left(\frac{dP}{dT}\right)^2 + 2\Delta(\alpha V)\frac{dP}{dT} + 3\mathcal{F}\frac{d^2E}{dT^2} - \frac{\Delta c_V}{T} - \Delta\left(\frac{\alpha^2 V}{\kappa}\right) = 0 \quad (12)$$

To simplify eq 12, we can reasonably neglect $\frac{d^2P}{dT^2}$ and assume $\Delta c_V \cong 0$ being both OLC and HOPG graphitic materials at the same quite high temperature where c_V is for both ones close to $\frac{3}{2}R$. Therefore, eq 12 becomes a quadratic equation in the 1st derivative with respect to T of the pressure:

$$\left(\frac{dP}{dT}\right)^2 - 2\frac{\Delta(\alpha V)}{\Delta(\kappa V)}\frac{dP}{dT} - \frac{1}{\Delta(\kappa V)}\left[3\mathcal{F}\frac{d^2E}{dT^2} - \Delta\left(\frac{\alpha^2 V}{\kappa}\right)\right] \cong 0 \quad (13)$$

The solution of eq 13 has been obtained by using the experimental data, $\frac{d^2E}{dT^2}$, and the knowledge of the T and P functions of the physical data of HOPG and OLC. The T functions are reported in Table 2 and their related coefficients given in Table 3. Unfortunately, α and κ data of OLC are unavailable and we utilized, as first approximation, the data of fullerene C_{60} [18]. Due to lack of data on the temperature dependency of the OLC molar volume, an estimation can be done starting from the definition of the isobaric expansion coefficient $\alpha(T) = \frac{1}{V}\left(\frac{\partial V}{\partial T}\right)_P$ and its T dependency reported in Table 2 together the coefficients for C_{60} given in Table 3. Therefore, equation below has been considered:

$$V(T) = V(T_0)\exp\left[\int_{T_0}^{T}(d_0 + d_1 T)dT\right] = V(T_0)\exp\left\{\Delta T\left[d_0 + \frac{d_1}{2}(T + T_0)\right]\right\} \cong V(T_0) \quad (14)$$

where $\left(T^2 - T_0^2\right) = \Delta T(T + T_0)$ holds. The final approximated value is justified by the amount in braces, which is $\cong 3\text{x}10^{-2}$ being $\Delta T = (T - T_0) \leq 700\text{K}$. The values of d_0 and d_1 are reported in Table 3. The $V(T_0)$ value was taken equal to 7.31×10^{-6} m^3 mol^{-1} at $T_0 = 298$ K which is the V^0 value of OLC [19]) (see Table 3). Due to the lack of data on the pressure dependence of α, κ and V^0 for OLC, all these parameters were considered constant with pressure for the carbon species present in both electrodes. This choice was mandatory to ensure a balanced behaviour to both OLC and HOPG. Figure 3 shows the trend of $\frac{d\Delta_r H_T}{dT}$ vs T in the left axis calculated according to eq 11 after solving eq 13 to find $\frac{dP}{dT}$, being the latter quantity plotted on the right axis. It should be noticed that the shape of the curve $\frac{dP}{dT}$ might be affected by the approximation $\frac{d^2P}{dT^2} \cong 0$ introduced in equation 12.

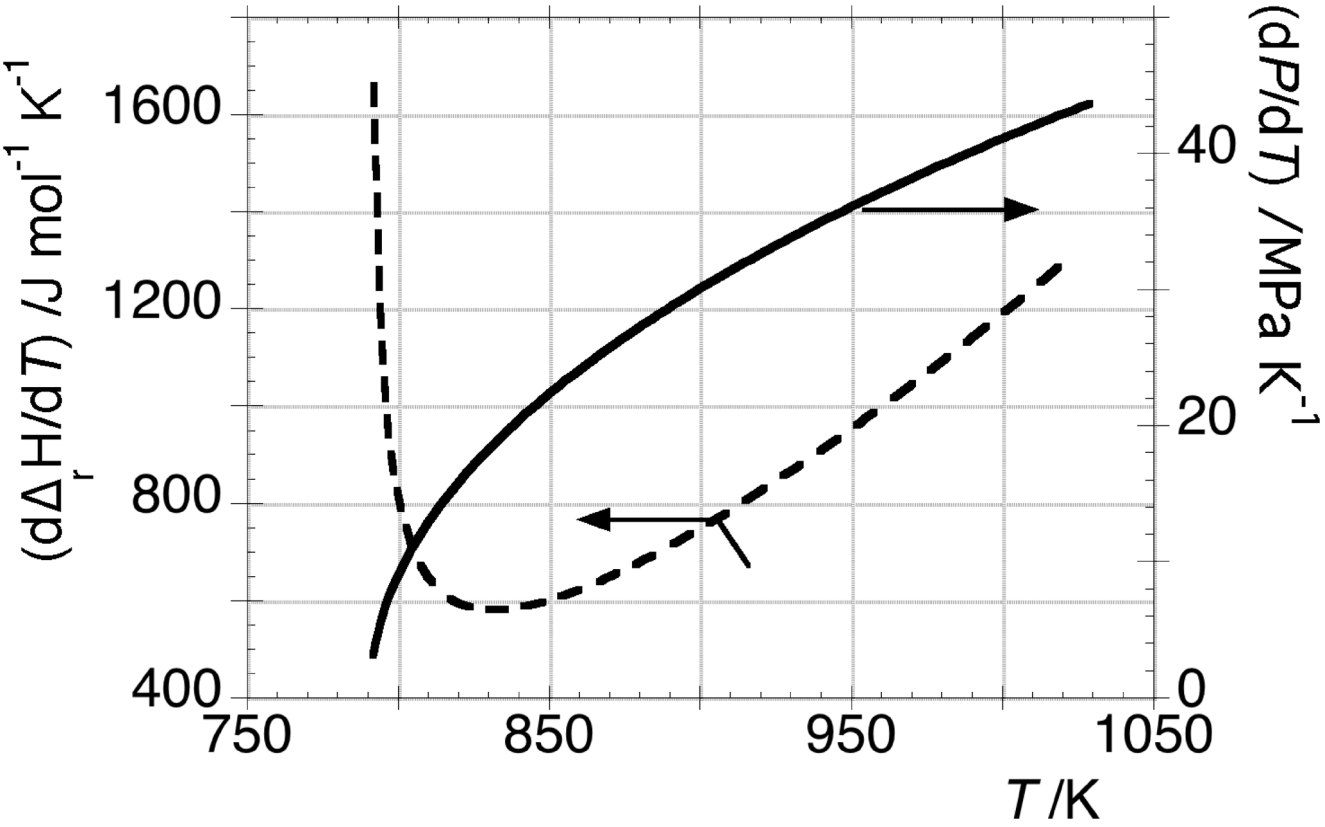

Figure 3. Representation of $\frac{dP}{dT}$ vs T obtained by solving eq 13 (right axis) and trend of $\Delta_r H(P,T)$ calculated by eq 11 (left axis).
doi:10.1371/journal.pone.0105788.g003

From the total differential of $\Delta_r H(T,P)$ the quantity $\left(\frac{\partial \Delta_r H}{\partial P}\right)_T = \frac{\frac{d\Delta_r H}{dT} - \left(\frac{\partial \Delta_r H}{\partial T}\right)_P}{\frac{dP}{dT}}$ can be obtained and plotted against T in Fig. 4 (right axis) together $\left(\frac{\partial \Delta_r H_T}{\partial T}\right)_P$ (left axis). Equation 4 was used for this calculation.

The entropy change of transformation B as function of temperature and pressure, was calculated as:

$$\Delta_r S(T,P) = [\Delta_r H(T,P) - \Delta_r G(T,P)]/T \qquad (15)$$

.This equation can be calculated through eq 7, after solving the quadratic eq 13, by using the experimental data of $\Delta_r G$ reported on Fig. 2. These thermodynamic functions are shown in Fig. 5. At 920.6 K, $\Delta_r H$ and $\Delta_r S$ values are 95.8 kJ mol^{-1} and 104.1 JK^{-1} mol^{-1}, respectively.

Why does the pressure change with temperature in our experiment? The experiment is carried out under high vacuum and the static pressure on the cell is maintained constant at about 0.1 bar as described in the experimental section (see § 1.3 of the Supporting Information S1). Thus, the present experimental conditions cannot justify the presence of the $\frac{dP}{dT}$ quantity. The explanation for $\frac{dP}{dT} >> 0$ should be searched in the growth of the pressure inside the cell, which is caused by a process occurring under volume constraint. The positive sign of *emf* indicates that $\mu(\mathrm{OLC}) > \mu(\mathrm{HOPG})$ where μ is the chemical potential of carbon. By itself this does not justify the increase of P with T but the trend of *emf* with T suggests it. Furthermore, there are experimental

Table 2. Temperature functions of the molar volume, V^0, isobaric volume expansion coefficient, α, and isothermal compressibility, κ, used for computing eq 13.

	$V^0(T)$[a]	$\alpha(T)$[b]	$\kappa(T)$[b]
HOPG[25]	$a_1 + a_2 T + a_3 T^2$	$\frac{a_2 + 2a_3 T}{a_1 + a_2 T + a_3 T^2}$	$(b_1 + b_2 T + b_3 T^2)^{-1}$
OLC	V^0	$d_0 + d_1 T$	$c_0 + c_1 T$

[a]Fullerene C_{60} data were assumed for OLC from reference [18] (see also text) with the exception of $\frac{dP}{dT}$, which is known [19].
[b]Linear equations for OLC (C_{60}) were taken up from the plots in reference [18].
doi:10.1371/journal.pone.0105788.t002

Table 3. Values of the coefficients of Table 2.

Coefficient [a]	Value	Ref.
a_1/m^3mol^{-1}	5.30×10^{-6}	[25]
$a_2/m^3\ mol^{-1}K^{-1}$	2.14×10^{-10}	[25]
$a_3/m^3\ mol^{-1}K^{-2}$	1.95×10^{-14}	[25]
b_1/Pa	3.63×10^{10}	[25]
$b_2/Pa\ K^{-1}$	-1.32×10^{7}	[25]
$b_3/Pa\ K^{-2}$	9.45×10^{3}	[25]
c_0/Pa^{-1}	8.37×10^{-11}	[18]
$c_1/Pa^{-1}K^{-1}$	7.66×10^{-15}	[18]
d_0/K^{-1}	4.30×10^{-5}	[18]
d_1/K^{-2}	4.27×10^{-9}	[18]
V^o/m^3mol^{-1}	7.31×10^{-6}	[19]

[a]The original values of coefficients α_i are given in nm^3. They were multiplied by 10^{-27} N_A being N_A the Avogadro number.
doi:10.1371/journal.pone.0105788.t003

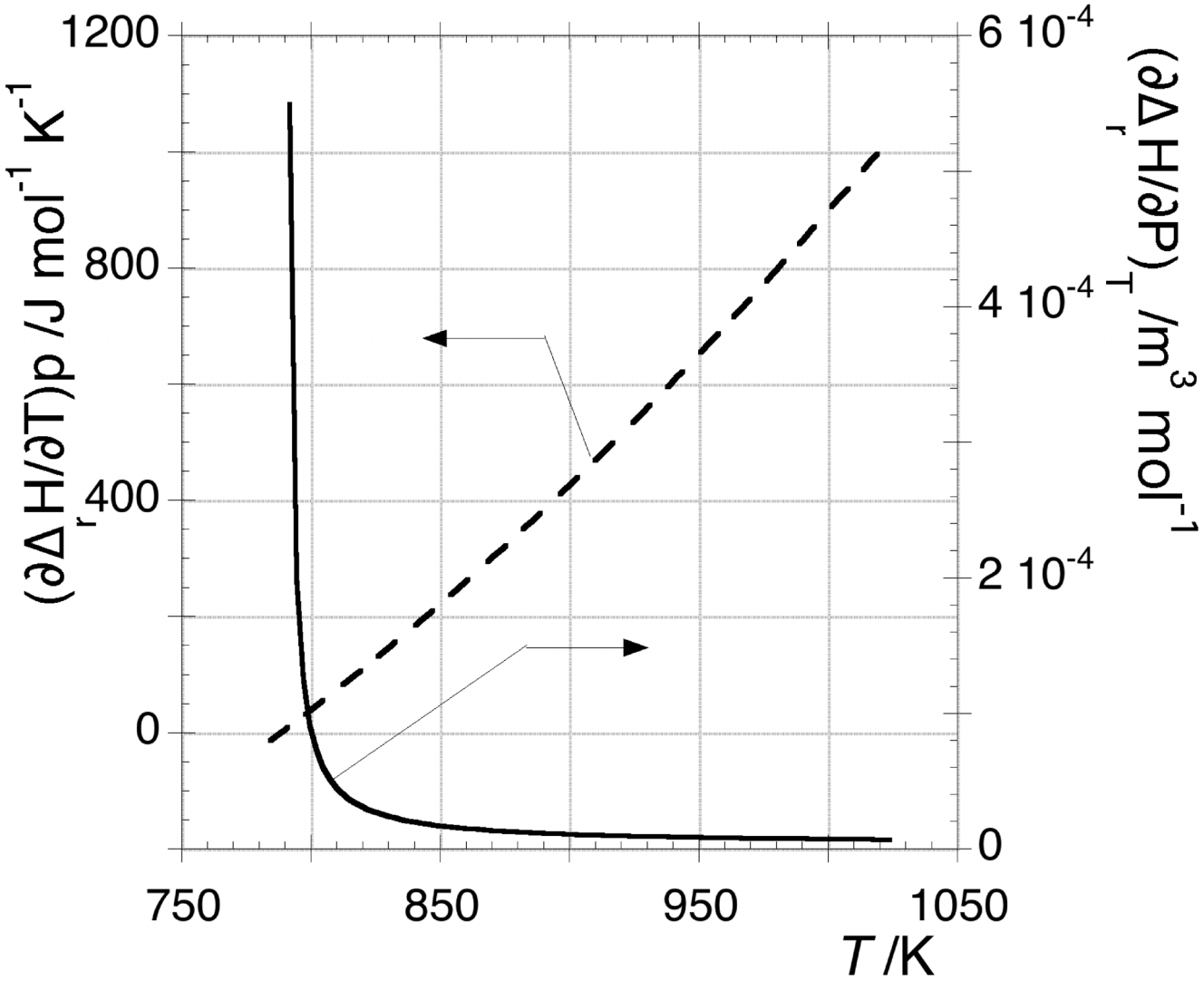

Figure 4. Partial derivatives of $\Delta_r H(P,T)$. The quantity in the left axis was calculated according to eq 4. The quantity in the right axis was calculated by the total differential of $\Delta_r H(P,T)$ through $\frac{dP}{dT}$ vs T function, obtained by solving eq 13.
doi:10.1371/journal.pone.0105788.g004

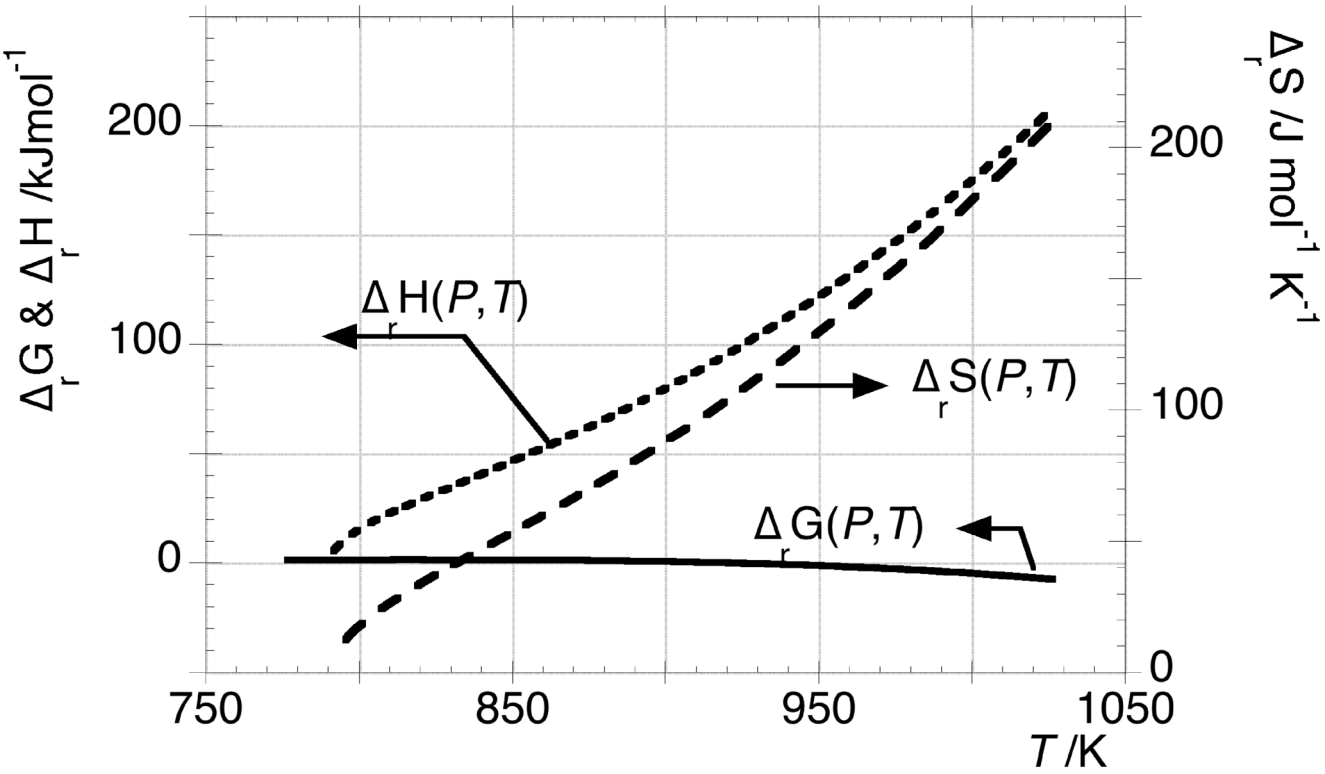

Figure 5. Representation on left axis of $\Delta_r H$ and $\Delta_r G$ vs T obtained respectively by eq 7, after solving quadratic equation 13, and eq 1. On the right axis, the trend of $\Delta_r S$ calculated by eq 15 is also displayed.
doi:10.1371/journal.pone.0105788.g005

evidences indicating that the electrode containing OLC is the site where the volume constraint is particularly high. They arise from the comparative analysis of both electrode powder mixtures, before and after the experiments, by making use of x-ray diffraction (XRD), micro Raman spectroscopy (mR) and high-resolution transmission electron microscopy (HR-TEM):

- The XRD patterns spectra demonstrate that no chemical change occurred (see §1.5.1 of the Supporting Information S1). The large increase of crystallinity of CrF_2 was the unique difference found in XRD. Due to their almost amorphous state, OLC give low intensity XRD features differently from HOPG, which is very well revealed. In the present case, the situation is complicated by the presence of features of other species in the electrode that superimpose and/or they are very close to the OLC features (see §1.1.2.2 of the Supporting Information S1). It is reported [20] in high temperature – high pressure experiments on OLC, that their most intense feature ($d_{200} = 0.354$ nm, $2\theta = 24.73^{\circ}$; see §1.1.2.2 of the Supporting Information S1) is negligibly shifted as function of pressure at constant T. For instance, at 500 °C the lattice parameter changes with pressure as -9.6×10^{-13} nmPa^{-1}. At our calculated pressures, which are in the order of tens of MPa (see below), a shift of $\cong 10^{-5}$nm is expected, which is clearly undetectable. The mR spectroscopy does not reveal differences (see §1.5.2 of the Supporting Information S1) with exception of some changes in the relative intensities, which are meaningless. There is superimposition of the OLC and HOPG features with the features of the mixture Cr_3C_2 - CrF_2 (see §1.1.2.3 of the Supporting Information S1). Therefore, though this inconvenient, the absence of any new feature is a proof that both carbon species remain unchanged;
- HR-TEM and STEM analyses show a very different scenario of the electrode powder with OLC before and after the experiments. Before, OLC are easy identifiable in the mixture as reported in the STEM image of Fig. 6A. Free OLC nanostructures (red arrows) are quite abundant, where they can be seen either as spots with very light contrast on the holey carbon grid or mixed with the Cr_3C_2-CrF_2 powder. The HAADF-STEM mode is also known as Z contrast mode because the intensity in each point of the image is proportional to Z^{α} with $\alpha \sim 2$ and Z the atomic number. Carbon appears dark, as it is much lighter than the other compounds present in these samples. The OLC morphology at the nanoscale is shown in Fig. 6B and is found in agreement with previous experimental results [7][21]. The inset in Fig. 6B shows the Fast Fourier Transform (FFT) of OLC where the reflections of graphitic planes appear quite diffuse.

The powder mixture of the same electrode after the experiment appears completely different: OLC are practically disappeared while large grains with round shaped contours were found as shown in the STEM image in Fig. 7A. Free OLC are hardly observable: just small pieces on the agglomerates, while the holey carbon grid is practically clean. The analysis on the very few OLC found in the sample reveals some significant differences with respect to the OLC before the experiment: the graphitic planes form now better ordered quasi-spherical structures (see Fig.7B). The electron energy loss spectroscopy measurements (see § 1.5.3. of the Supporting Information S1) agree with this result: the sp^2 carbon coordination values were found 82±3% and 86±3% for

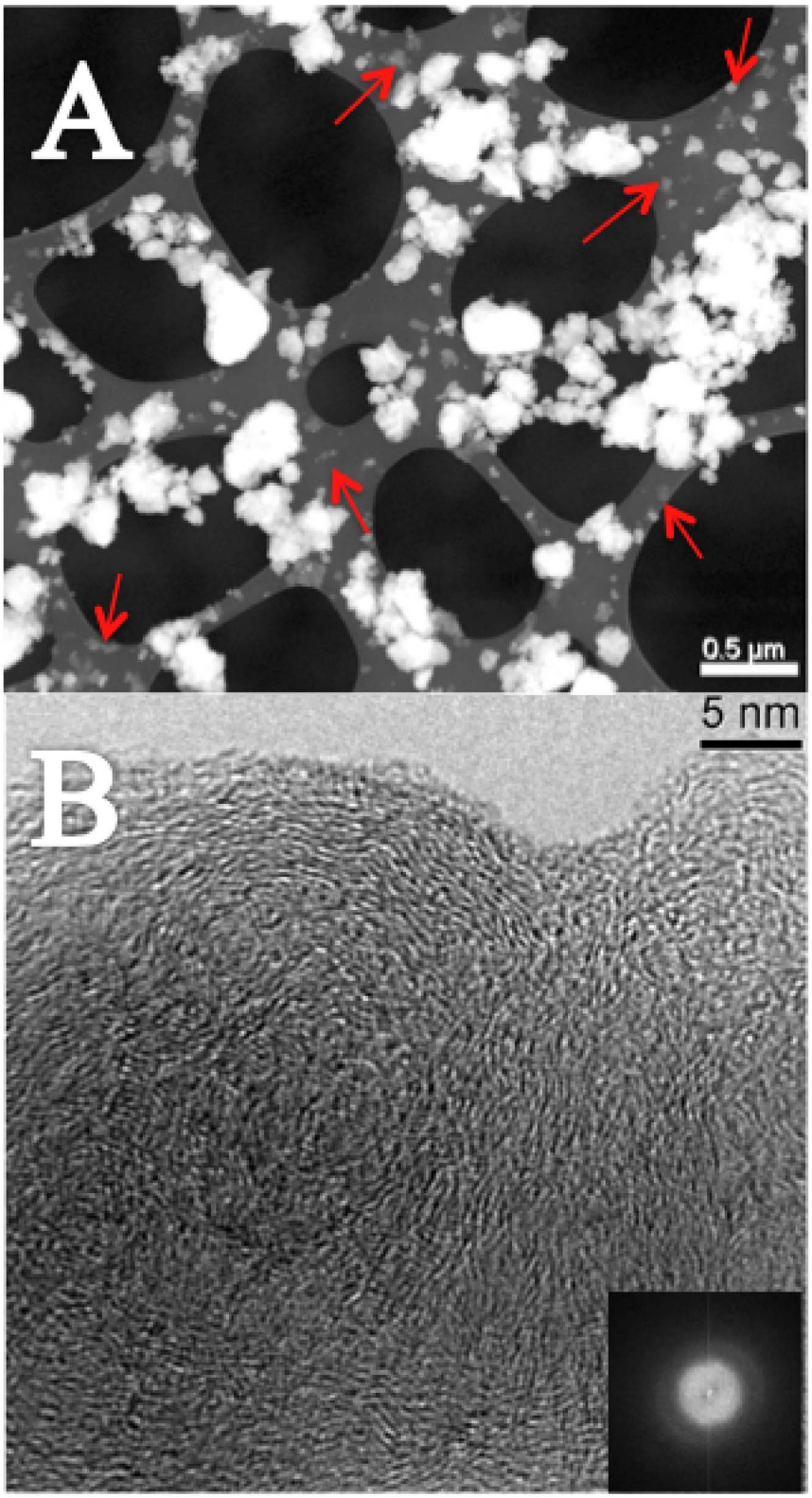

Figure 6. Before the experiment. Panel A: STEM image of the powder of the electrode containing OLC. The OLC nanostructures appear on the holey carbon grid as spot with very light contrast. Some of them are indicated with red arrows. Panel B: HR-TEM of OLC. The FFT image in the inset shows poor crystallinity of OLC.
doi:10.1371/journal.pone.0105788.g006

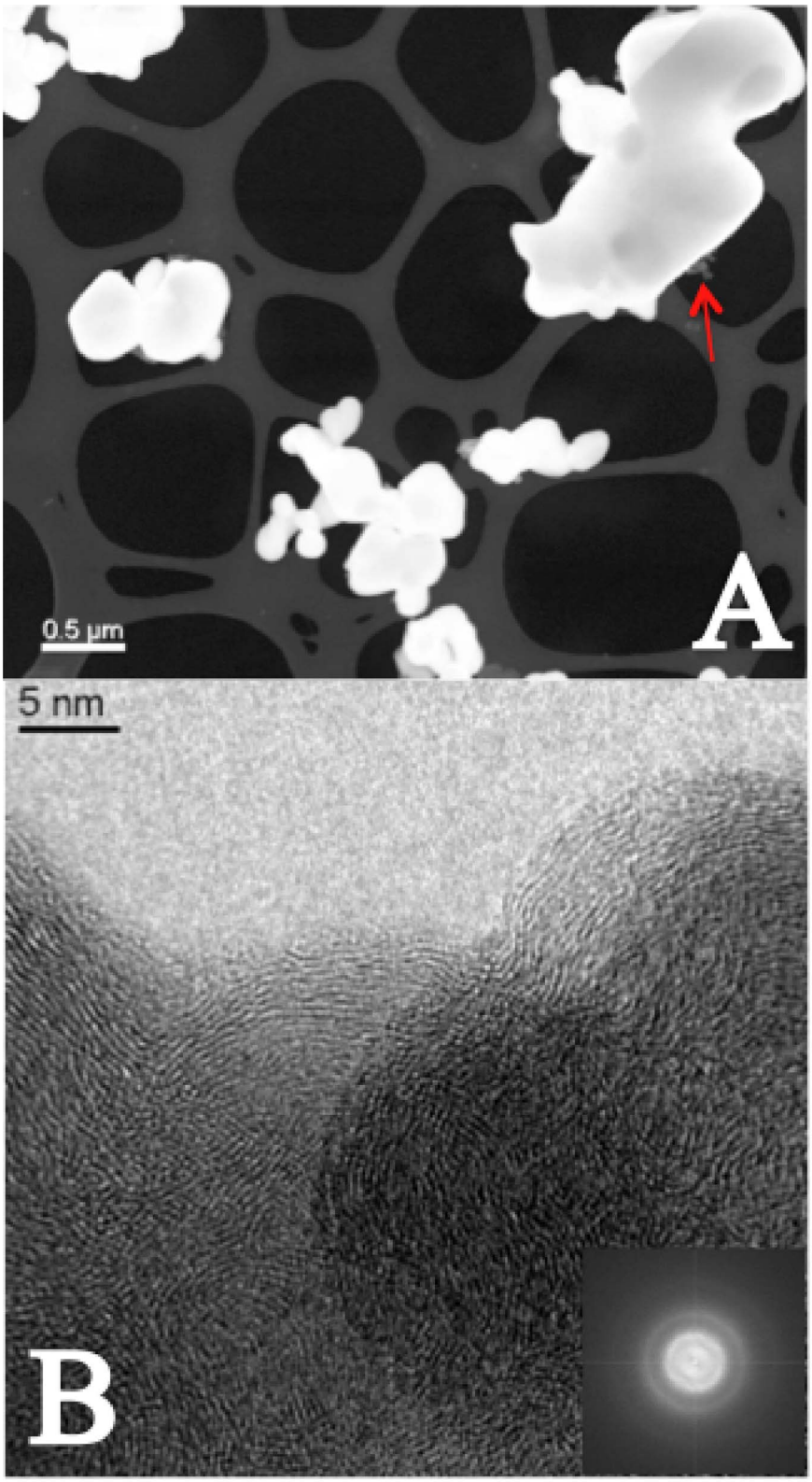

Figure 7. After the experiment. Panel A: STEM image of the powder of the electrode containing OLC. The OLC nanostructures are practically disappeared. The holey carbon grid is clean and only large grains with rounded shape stay on the grid. A few visible OLC are indicated with red arrow. Panel B: HR-TEM of OLC. The FFT image in the inset shows that the crystallinity of OLC is higher with respect to the FFT image in Figure 6B.
doi:10.1371/journal.pone.0105788.g007

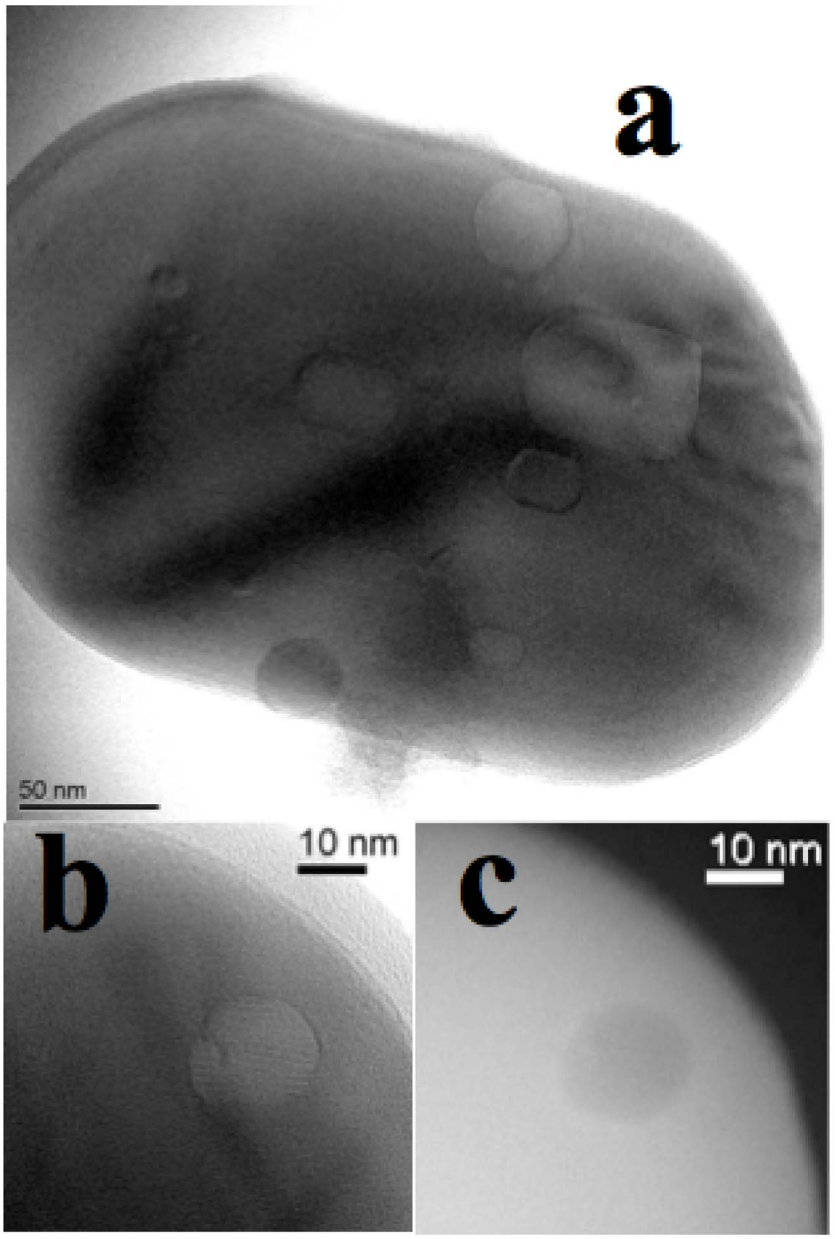

Figure 8. Zero loss TEM image (Panel a) of a typical small sintered particle (as the particles in Figure 7A) of the electrode with OLC after the experiment. The particle contains several cavities, that can be empty, or at least full of material much lighter than the surrounding sample, as it is proven by the comparison between the HRTEM (panel **b**) and STEM (panel **c**) images of the same cavity, that is whiter in **b** and darker in **c**.
doi:10.1371/journal.pone.0105788.g008

OLC before and after, respectively and the result seems to point to a further graphitization of OLC towards multishell ordered structures in the process (see discussion below). The sintered agglomerates usually are so thick to result non-transparent to electrons and to prevent the analysis of their internal structure. When small particles are found, the EELS revealed typical features of variable size inside the particle. Their contrast is typical of cavities, but it was not possible to assess whether they are empty or possibly filled with OLC. This is the most reasonable hypothesis, being OLC otherwise missing.

The zero loss TEM image of a typical small sintered particle containing several cavities is shown in Fig. 8a. The fact that these cavities are empty or filled with material lighter than the surrounding sample is proven by the comparison between the HRTEM and STEM images in Fig. 8b and Fig. 8c of the same cavity, that is whiter in b and darker in c.

The electrode containing HOPG and the same Cr_3C_2 - CrF_2 mixture does not show any modification after the experiment, as it can be seen by comparing the STEM images in Fig.9 A and B.

The following considerations arise from the above evidences:

- The temperature range explored in the experiments does not allow suspecting any vaporization of carbon from OLC. The C-nanostructures are still in the electrode;
- High temperatures and experiments lasting hundreds of hours create the ideal conditions to favour the sintering of the whole

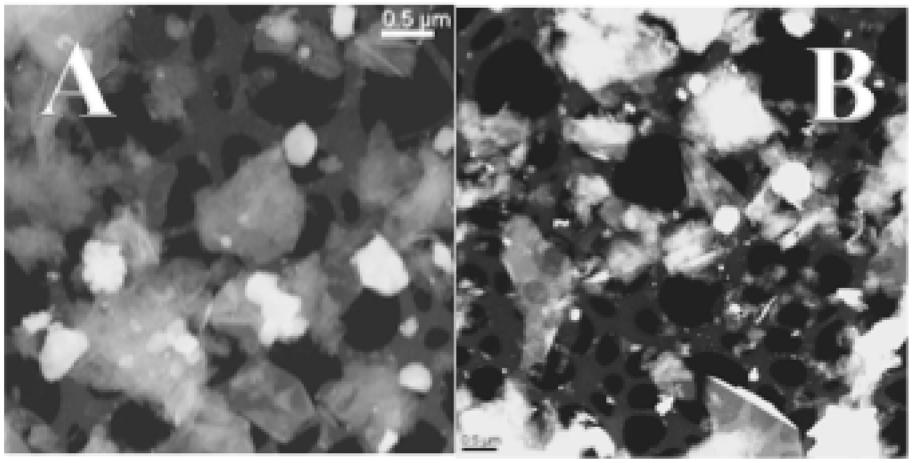

Figure 9. STEM images of the electrode containing HOPG. Panel A, **before the experiment**. Panel B, **after the experiment**. No differences were found and no sintering was observed.
doi:10.1371/journal.pone.0105788.g009

mixture where OLC remain embedded in the very hard and refractory structure of Cr_3C_2. The melting points of Cr_3C_2 and CrF_2 are respectively 2168 and 1167 K. The highest temperature reached in the experiments was 1030 K, which is close to the melting point of CrF_2. Thus, it is expected that its softening acts as a sintering medium of the whole mixture. The high specific surface area of OLC (>100 m^2g^{-1}, see § 1.1.1 of the Supporting Information S1) contributes to this process and facilitates the embedding of the nanostructure. Therefore, the role of OLC nanoparticles seems to be crucial and it explains the absence of any modification of the electrode containing HOPG (and the same Cr_3C_2-CrF_2 mixture) which worked in the same experimental conditions;

- Consider as rough approximation the electrodes as cylinders free of expanding with temperature filled with rigid particles (sintered Cr_3C_2-CrF_2 mixture) embedding nanoparticles (OLC) the dilatation of which is hindered. By imposing no volume change for both OLC and HOPG, the respective $\frac{dP}{dT} = \frac{\alpha}{\kappa}$ values can be evaluated and compared as follows:

$$\left.\frac{dP}{dT}\right|_{O} = \left(\frac{\alpha}{\kappa}\right)_{O} \cong 0.5\,\mathrm{MPaK^{-1}}; \left.\frac{dP}{dT}\right|_{H} = \left(\frac{\alpha}{\kappa}\right)_{H} \cong 8\,\mathrm{PaK^{-1}} \quad (16)$$

The subscripts O and H stand for OLC and HOPG. The temperature dependence of the quantities entering eq 16 has been neglected in the computation and the coefficients a_2, b_1, c_0 and d_0 were only retained in the expression reported in Table 3. The values found in eq 16 demonstrate clearly the great difference in the internal pressures to which both carbon forms are subjected in the respective electrodes. For the sake of comparison, the quantity $\frac{dP}{dT}$ for Cr_3C_2 is: $\left.\frac{dP}{dT}\right|_{Cr} = \left(\frac{\alpha}{\kappa}\right)_{Cr} \cong 3.4\,\mathrm{MPaK^{-1}}$ where κ [22] and α [23] are available in literature. Due to the negligible changes with temperature of the internal pressure (see eq 16), the chemical potential of carbon in HOPG, μ_H, is only a function of T differently to the chemical potential of carbon in OLC, μ_O, that is a function of T and $P(T)$. Therefore, we can write that:

$$\Delta_r G(T,P) = \mu_O[T,P(T)] - \mu_H(T). \quad (17)$$

Evaluation of the surface contribution

Owing to the nanometric size of the carbon particles, the surface contribution to the energetics of the process cannot be neglected, in principle. In the following of this section the shape of the nanoparticle is assumed to be spherical. Let us estimate the chemical potential difference using the thermodynamic approach, based on the Gibbs model for interface [24], in terms of bulk chemical potential, surface free energy and surface tension.

The difference between surface energy and surface tension plays a fundamental role when dealing with interphases in the solid state. In this respect, we briefly recall the definition of these quantities, which are needed for the discussion that follows. The surface energy excess, σ, is the reversible work required to create a unit surface at constant volume, temperature, pressure and composition [24]. In such a process the surface is not stretched during its formation. On the other hand, the surface tension, γ, is defined as the reversible work (per unit area) required to change the area of the surface through a stretching process. It is worth noticing that in this definition the infinitesimal deformation of the surface involves an "initial" configuration of the system where the solid is not stressed. By including bulk and surface contributions, the general expression of the chemical potential difference reads (see §2 of the Supporting Information S1)

$$\Delta_r G(T) = \Delta\mu_B + \Delta\mu_S = \Delta\mu_B + \frac{2V}{r}\left(\sigma - \frac{\kappa\gamma^2}{3r}\right) \quad (18)$$

where r is the radius of the nanoparticle and $\Delta\mu_B$ denotes the "bulk" contribution, that is $\Delta\mu_{r\to\infty}$. In the following we focus our attention on the impact of the surface term ($\Delta\mu_S$) on $\Delta_r G(T)$ and on its temperature dependence.

The contribution of the surface tension containing term to $\Delta\mu_S$ is usually smaller than that due to the surface excess free energy, $\frac{2V\sigma}{r}$. Consequently, $\Delta\mu_S$ is expected to be higher than zero. Typical values of the quantities entering eq 18 are [25]

$V = 5.36\times10^{-6}$ m^3 mol^{-1}, $\kappa = 3.24\times10^{-10}$ Pa^{-1} and $r = 10$ nm. As far as the σ value is concerned, for nanocarbon structures, such as fullerene, single and multi walled nanotubes, it is found [5] to range between 0 and 0.045 Jm^{-2}. On this basis, the upper bound of $\Delta\mu_S \cong \frac{2V\sigma}{r}$ is estimated to be about 50 Jmol^{-1} for $r = 10$ nm.

As far as the temperature dependence of $\Delta\mu_S$ is concerned, it is ascribed to the temperature dependence of the physical quantities entering in eq 18. In particular, the temperature dependence of σ is given by the Gibbs adsorption equation that, for one component system, implies $\frac{d\sigma}{dT} = -s^x$, where $s^x = S^x/A$ is the excess surface entropy. From this equation, neglecting as a first approximation the temperature dependence of the excess entropy in the temperature range here considered, we get $\sigma(T) = -s^x(T - T^*) + \sigma*$ where T^* is the temperature at which $\Delta_r G(T) = 0$. Concerning the temperature dependence of the surface tension, given by eq 1 in the Supporting Information S1 (§ 2), it is obtained

$$\frac{d\gamma}{dT} = -s^x - A\frac{d_s s^x}{d_s A} + \frac{2}{3}\alpha\gamma \qquad (19)$$

where we exploit the fact that the surface energy is a function of the independent variables temperature and "stretched area" A (the subscript s stands just to remind us that the variation is performed by stretching). According to the discussion that follows this derivative can be estimated using the Born-Stern method [26]. In this approach, the entropy excess per unitary area of a solid-vacuum interface is equal to $s^x = \frac{1}{A}\left(S - S'\right) = \rho_a\left(s_1 - s_1'\right)$ where S is the entropy of the actual solid, S' the entropy of the model system (without interface), ρ_a the surface density and $s_1\left(s_1'\right)$ the entropy, per atom, of surface (bulk) species. By assuming, as usual, $\left(s_1 - s_1'\right)$ independent of temperature and deformation of the surface $\frac{d_s A}{A}$, for $\frac{d_s\rho_a}{d_s A} = -\frac{\rho_a}{A}$ one obtains $\frac{d\gamma}{dT} = -s^x - A\left(s_1 - s_1'\right)\frac{d_s\rho_a}{d_s A} + \frac{2}{3}\alpha\gamma \cong \frac{2}{3}\alpha\gamma$. For instance, by considering the excess entropy equal to the change in the vibrational entropy of the atom the expression $s^x \cong k\rho_a \ln\frac{v_\perp}{v_\perp'}$ holds where $v_\perp'(v_\perp)$ is the vibrational frequency of the surface (fully coordinated) atom along the "broken bond" direction. Since for the number of mole of atoms in the particle, N, is constant we set $\frac{r^3}{V} = \frac{3}{4\pi}N = b^{-1}$ in eq 18 to obtain $\Delta\mu_S = 2br^2\left(\sigma - \frac{\kappa\gamma^2}{3r}\right)$. Moreover,

$$\frac{d\Delta\mu_S}{dT} \cong -2\frac{V}{r}\left[s^x - \frac{\alpha}{3}\left(2\sigma - \frac{5}{3}\frac{\kappa\gamma^2}{r}\right)\right] \qquad (20)$$

where α is of the order of 10^{-6} K^{-1}. A crude estimate of the vibrational contribution of s^x, on the basis of the Kossell model [26] shows that $s^x > k\rho_a \ln\sqrt{2}$ that implies, using $\rho_a = \rho_g^{\frac{2}{3}}$ with ρ_g

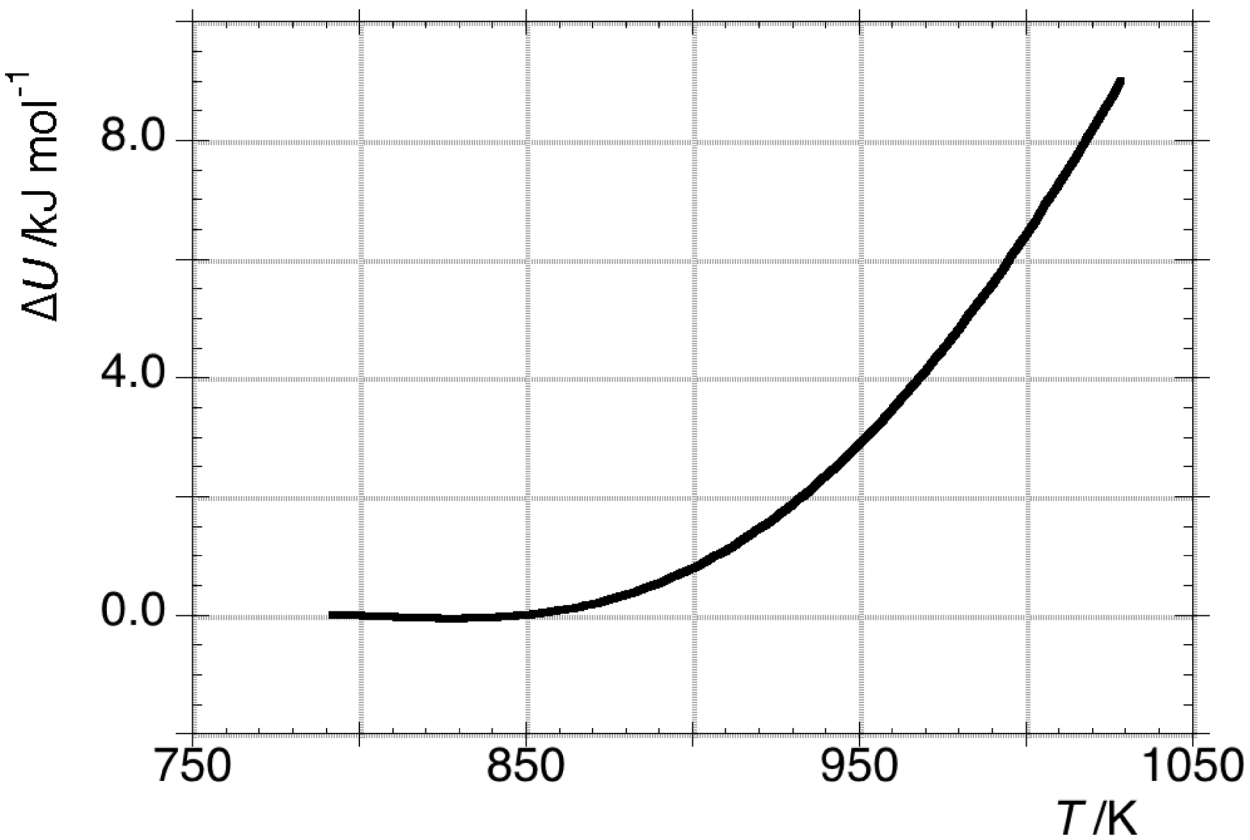

Figure 10. The change of internal energy $\Delta U[T,P(T)]$ of OLC is reported against temperature according to eq 22.
doi:10.1371/journal.pone.0105788.g010

the graphite density, a value of $s^x \geq 10^{-4}$ J m^{-2} K^{-1}. This figure is about two orders of magnitude larger than α. Moreover, $(2Vs^x/r)_{r=10\text{nm}} \geq 0.1$ J mol^{-1} K^{-1}. From eq 15, the value of $\Delta_r S(P,T)$, in the middle of temperature range, is equal to 96.75 Jmol^{-1}K^{-1}, which is not consistent with the value $(-2Vs^x/r)$.

The present analysis indicates that the bulk term is the dominant contribution both to the chemical potential change of transformation B and its derivative on T. At this point, a comment is in order on the use of the Gibbs model for dealing with OLC systems. In fact, in this approach "bulk" and surface terms sum up as two independent contributions where the "size effect" is usually contained in the surface term only, i.e., $\Delta\mu_B = \Delta\mu_{r\to\infty}$ is independent of r. On the other hand - still remaining in the framework of the Gibbs model - owing to the variable curvature of the sheets, which made up the nanoparticles, in the OLC the "bulk" term has to be considered a function of the particle radius. For this reason in the following we refer to "atomistic" approaches for determining the energetics of the OLC particles. In fact, in these methods a suitable interaction potential functions for the C atoms is used and this makes it possible to estimate $\Delta\mu_B$ as a function of r.

Now we focus our attention on the internal energy of the particle due to the isothermal transformation from a relaxed state at internal energy U_0 and volume V_0 to a stressed state at U and V. To do this the *energy equation*, namely

$$\left(\frac{\partial U}{\partial V}\right)_T = T\left(\frac{\alpha}{\kappa}\right) - P \tag{21}$$

was utilized. The integration of eq 21 gives the change of internal energy as (see §3 of the Supporting Information S1):

$$\Delta U = (U - U_0)_T = \frac{V^0}{\kappa}\left\{\left[1-(1+\kappa P)e^{-\kappa P}\right] + \alpha T\left(e^{-\kappa P}-1\right)\right\} \tag{22}$$

The value of V^0, α and $\kappa\kappa$ are given in Tables 2 and 3. The pressure as function of T was obtained by numerical integration of $\frac{dP}{dT} = f(T)$ assuming $P = 0$ at $T = 776.6$ K, which was the lowest experimental temperature. The resulting function satisfies the relationship $P = m_0 + m_1 T + m_2 T^2 + m_3 T^3$where $m_0 = 1.2947\times10^6$ bar; $m_1 = -4187.2$ bar K^{-1}; $m_2 = 4.2571$ bar K^{-2}; $m_3 = -1.3067\times10^{-3}$ bar K^{-3} with correlation coefficient 0.9999. At the highest temperature, the maximum pressure value is about 70 kbar. The trend of $\Delta U[T,P(T)]$ with temperature, which is almost perfectly quadratic, is plotted in Fig. 10.

It is worth noticing that the $\Delta U[T,P(T)]$ values and its trend with temperature are not comparable with values and trend of $\Delta_r H(P,T)$ reported in Fig. 5. For example, at 903 K, which is the temperature in the middle of the explored temperature interval, the ratio $\frac{\Delta_r H(P,T)}{\Delta U[T,P(T)]} \cong 10^2$.

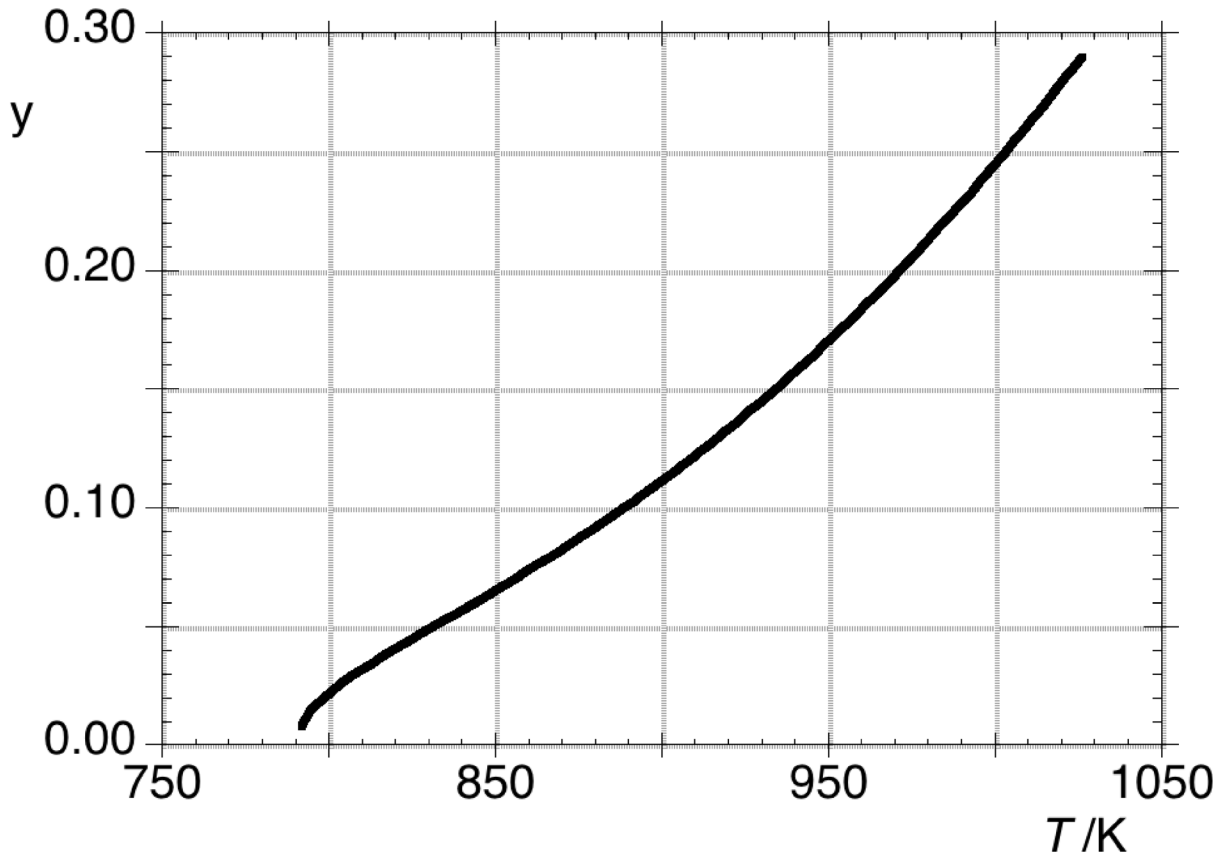

Figure 11. Trend of the change of the fraction of C defects in OLC against *T*. One assumes that the real transformation involves equilibrium $C_{HOPG} = C_{OLC_x} = yC_{ad} + C_{OLC_{x-y}}$ and y is calculated by eq 23.
doi:10.1371/journal.pone.0105788.g011

Due to such a high ratio jointly to the very small surface contribution, we assume that as a consequence of the high internal pressure another process connected to B should be considered. We are likely dealing with a reversible process that requires the formation of C defects in OLC, probably already defective. Thus, the whole process determining the *emf* of the cell could be written as:

$$C_{HOPG} = C_{OLC_x} = yC_{ad} + C_{OLC_{x-y}} \quad (B1)$$

instead of process B.

Obviously, this implies that the previously considered relation $\Delta_r G = \mu_O - \mu_H$ should be written as $\Delta_r G = <\mu_O> - \mu_H$ where $<\mu_O>$ is the mean chemical potential of carbon atoms in the electrode containing the OLC nanostructures. In this quantity, the C atoms formed should be considered adsorbed atoms, C_{ad} the formation of which causes dangling bonds. A rough evaluation of the defect fraction in equilibrium B1 can be evaluated through equation:

$$y = \frac{\Delta_r H(P,T) - \Delta_f H_{O_{x-y}}}{\Delta_f H_C} \cong \frac{\Delta_r H(P,T)}{\Delta_f H_C} \quad (23)$$

where $\Delta_f H_C$ and $\Delta_f H_C$ are the enthalpy of formation per carbon atom of defective OLC and free carbon atom (7.43 eV at 298 K) [27], respectively. The quantity $\Delta_f H_{O_{x-y}}$ depends on the number of shells as described for multishell fullerene (MSF) made of concentric circumspheres of polyhedra C_n (I_h, $n = 60k^2$) and C_n (I_h, $n = 180k^2$) where $k = 1,2$ up to L is any positive integer representing the number of shells. I_h and n are respectively the symmetry group and number of C atoms. According to the literature [28], the quantity $\Delta_f H_{O_{x-y}}$ is of the order of magnitude of meV and therefore it is negligible when compared to $\Delta_r H(P,T)$ which is about 1 eV. Even the formation energy of a single carbon shell starting from graphene implies negligible energy values ranging from 331 to 34 meV at^{-1} for C_{60} and C_{960}, respectively (see J. Bernholc et al. [3]). As stated in the above reference, the authors showed that the larger the size of the shell, the lower the energy of formation. Figure 11 shows how y changes with T.

Due to the assumption for obtaining eq 23, the trend of y is the same as $\Delta_r H(P,T)$ shown in Fig. 5. Anyway, the value of y is likely consistent with a change corresponding to one or more OLC shells. The experimental evidence through the *emf* vs T data shows that this process occurs reversibly. In addition, defects imply the formation of dangling bonds, which also contribute to the increase of the entropy change.

Conclusions

In the present experimental work, we obtained high temperature data of the stability of onion-like carbon with respect to highly oriented pyrolytic graphite. Since this was performed in reversible way, through the *emf* measurement of a galvanic cell, the quantities related to the transformation investigated have to be considered reliable thermodynamic data.

The evidence that in the operating conditions the *emf* data cannot be only function of temperature allowed measuring the changes of the chemical potential of carbon in OLC under volume constraint. The volume constraint is reasonably proven by the HR-TEM images where the rigid cages made of sintered CrF_2–Cr_3C_2 mixture likely embed OLC.

The positive value of $\Delta_r S$ and its increase with temperature indicate that the OLC is a nanostructured system with a large number of defects. The change of their fraction with T was evaluated. The present analysis indicates that the bulk term is the dominant contribution to both chemical potential and entropy change of the transformation.

The absence of any chemical change in the electrodes after hundreds hours of work at high temperature guarantees the whole reliability of the experiments.

Supporting Information

Supporting Information S1
(DOC)

Acknowledgments

This work was partially financed through the PRIN 2009 Project no. 2009N4BJ4J and "Acquisizione di medie e grandi attrezzature scientifiche 2010" Università di Roma *La Sapienza*, no. C26G10KKK5.

Author Contributions

Conceived and designed the experiments: AL D. Gozzi. Performed the experiments: AL D. Gozzi LL GB D. Gazzoli LB. Analyzed the data: D. Gozzi MT. Contributed reagents/materials/analysis tools: AL. Contributed to the writing of the manuscript: D. Gozzi MT. Galvanic cell and experiment preparation, emf measurements, data elaboration: AL LB D. Gozzi. Evaluation of surface contribution and discussion of results: MT. HRTEM and EELS measurements: LL GB. microRaman measurements: D. Gazzoli.

References

1. Gozzi D, Latini A, Lazzarini L (2009) High-temperature determination of surface free energy of copper nanoparticles. J Am Chem Soc 131: 12474–12482.
2. Tomanek D, Zhong W, Krastev E (1993) Stability of multishell fullerenes *Phys Rev B* 48: 15461–15464.
3. Bernholc J, Brabec CJ, Maiti A, Yi J-Y (1994) Structural transformations, reactions, and electronic properties of fullerenes, onions, and buckytubes. Comp Mat Science 2: 547–556.
4. Girifalco LA, Hodak M, Lee RS (2000). Carbon nanotubes, buckyballs, ropes, and a universal graphitic potential. Phys Rev B 62: 13104–13110.
5. Jiang Q, Chen ZP (2007) Thermodynamic phase stabilities of nanocarbon. Carbon 44: 79–83.
6. Barnard AS (2006) Theory and modeling of nanocarbon phase stability. Diamond & Related Mat 15: 285–291.
7. Banhart F, Ajayan PM (1996) Carbon onions as nanoscopic pressure cells for diamond formation. Nature 382: 433–435.
8. Banhart F, Füller T, Redlich Ph, Ajayan PM (1997) The formation, annealing and self-compression of carbon onions under electron irradiation. Chem Phys Lett 269: 349–355.
9. Sun L, Banhart F (2006) Graphitic onions as reaction cells on the nanoscale. Appl Phys Lett 88: 193121–193123.
10. Latini A, Gozzi D, Ferraris G, Lazzarini L (2011) High-temperature resistivity of dense mats of single-walled carbon nanotube bundles. J Phys Chem C 115: 11023–11029.
11. Latini A, Tomellini M (2009) Thermodynamics of CVD synthesis of multiwalled carbon nanotubes: a case study. J Phys Chem C 113: 45–53.
12. Gozzi D, Iervolino M, Latini A (2007) The thermodynamics of the transformation of graphite to multiwalled carbon nanotubes. J Am Chem Soc 129: 10269–10275.
13. Shenderova OA, Zhirnov VV, Brenner DW (2002) Carbon nanostructures. Crit Rev Solid State Mater Sci 27; 227–356.
14. Kuznetsov VL, Chuvilin AL, Butenko YV, Mal'kov IY, Gutakovskii AK, et al. (1994) Study of onion-like carbon OLC formation from ultra disperse diamond (UDD). Mater Res Soc Symp Proc 359: 105–110.
15. Lee RKF, Hill JM (2012) General formulae for interacting spherical nanoparticles and fullerenes. J Math Chem 50: 1289–1303.
16. Zaiser M, Banhart F (1997) Radiation-induced transformation of graphite to diamond. Phys Rev Lett 79: 3680–3683.
17. Klotz IM, Rosemberg RM (2008) Chemical Thermodynamics. 7th Edition, John Wiley & Sons, Inc., Publishing, p. 200.
18. Girifalco LA (1995) Extended Mie-Grüneisen theory applied to C60 in the disordered fcc phase. Phys Rev B 52: 9910–9916.

19. Sano N, Wang H, Alexandrou I, Chhowalla M, Teo KBK, et al. (2002) Properties of carbon onions produced by an arc discharge in water. J Appl Phys 92: 2783–2788.
20. Dubitsky GA, Serebryanaya NR, Blank VD, Skryleva EA, Kulnitsky BA, et al. (2011) Effect of high pressures and temperatures on carbon nanoonion structures: comparison with C60. Russ Chem Bull Int Ed 60: 413–418.
21. Welz S, McNallan MJ, Gogotsi Y (2006) Carbon structures in silicon carbide derived carbon. J Mat Proc Tech 179: 11–22.
22. Chao J (2008) First-principles study of structural, elastic, and electronic properties of chromium carbides. Appl Phys Lett 92: 041909–041911.
23. Scabarozi TH, Amini S, Leaffer O, Ganguly A, Gupta S, et al. (2009) Thermal expansion of select $Mn+1AXn$ M = early transition metal, A = A group element, X = C or N) phases measured by high temperature x-ray diffraction and dilatometry. J Appl Phys 105: 013543–0135410.
24. Shuttleworth R (1950) The Surface Tension of Solids. Proc Phys Soc (London) A 63: 444–457.
25. Colonna F, Fasolino A, Meijer EJ (2011) High-pressure high-temperature equation of state of graphite from Monte Carlo simulations. Carbon 49: 364–368.
26. Mutaftschiev B (2001) The atomistic Nature of Crystal Growth. Springer-Verlag.
27. IVTANTHERMO for Windows, v.3.0; database of thermodynamic properties of individual substances and thermodynamic modeling software; Glushko Thermocenter of RAS: 2005
28. Tang AC, Huang FQ (1995) Theoretical studies of multishell fullerenes. Phys Rev B 52: 17435–17438.

Supporting Information

High Temperature Stability of Onion-like Carbon vs Highly Oriented Pyrolytic Graphite

Alessandro Latini[1], Massimo Tomellini[2], Laura Lazzarini[3], Giovanni Bertoni[3], Delia Gazzoli[1], Luigi Bossa[1] and Daniele Gozzi[1]*

LEGEND

---

1. Dipartimento di Chimica, Università di Roma *La Sapienza*, Roma, Italy
2. Dipartimento di Scienze e Tecnologie Chimiche, Università di Roma *Tor Vergata*, Roma, Italy
3. IMEM – CNR, Parma, Italy

1.

1. **Starting materials for the electrode preparation**

1.1. Information on HOPG, OLC, Cr_3C_2, CrF_2 as received.

	Purity /%	Size	Maker
HOPG[a]	99.3	—	Momentive Performance, Materials, Inc. (Germany)
OLC[b]	≥ 99	< 30 nm	Sigma-Aldrich
Cr_3C_2	99	325 mesh	Sigma-Aldrich
CrF_2	97	80 mesh	Chempur (Germany)

[a] ZYH grade, mosaic spread 3.5°±1.5°. Powder obtained by exfoliating a piece of 20x20x4 mm.

[b] Prepared by laser ablation of graphite. The specific surface area is > 100 m^2g^{-1}. The as received powder was two times treated in refluxing HCl ~6 M to remove possible metallic contaminants then washed thoroughly with deionized water until neutral pH of the washings.

1.2. Characterization

All the figures below show the characterization of all as received substances utilized in the electrodes of the galvanic cell.

1.2.1. Thermogravimetry (TG) and Differential Thermal Analysis (DTA).

Thermogravimetric measurements were performed by a Netzsch STA 409 PC Luxx thermobalance (temperature range: RT to 1500 °C; resolution: 2 μg)

Figur OPG and
OLC ses. The
puriti ely.

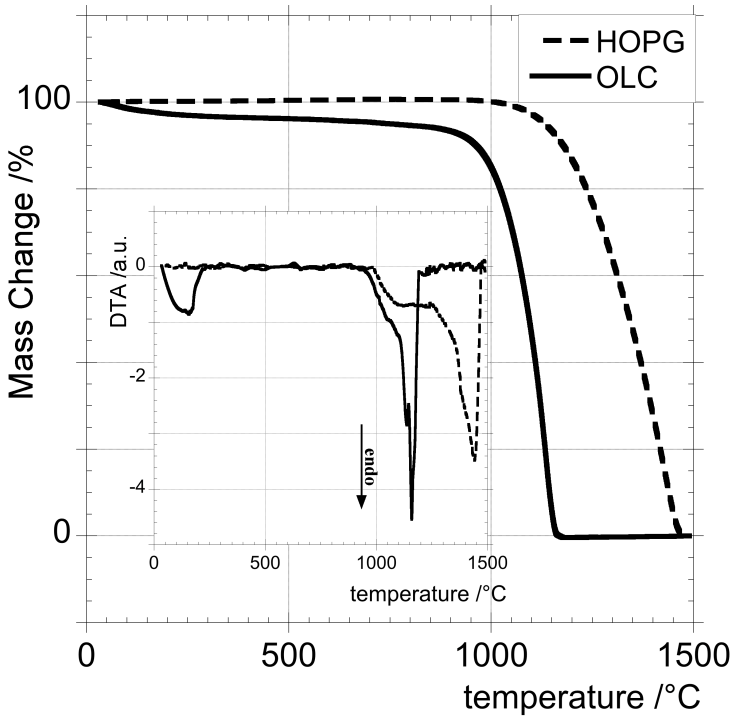

in simultaneous DTA-TG mode. Temperature was measured by means of a S-type thermocouple (Pt-Pt/Rh 10%). The thermocouple was calibrated against the melting points of In, Sn, Bi, Zn, Al, Ag, Au and Ni. All the measurements were performed in

alumina crucibles with a scan rate of 5 °C min^{-1}, under a flow of pure CO_2 (80 ml min^{-1} @ 1.013 bar and 21 °C). A correction measurement without sample was performed and subtracted to the TG and DTA curves of the samples. The purities found through TG for HOPG and OLC are 99.32 and 99.99 w%, respectively. The DTA curves for both materials are shown in the inset.

1.2.2. x-ray diffraction (XRD)

Figure S2. X lectrodes of cell
A. From th features were
checked with

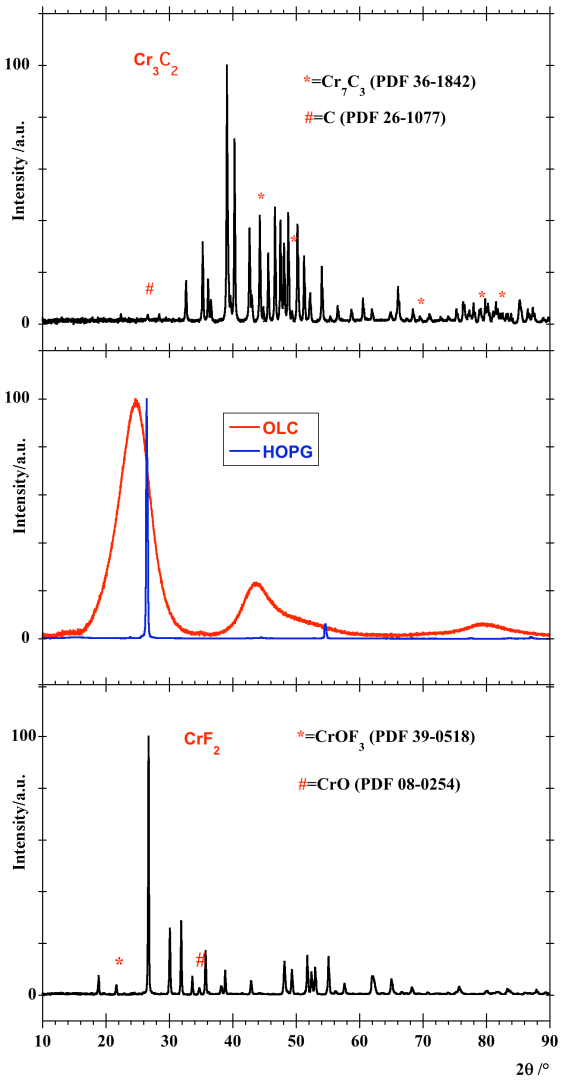

Diffraction patterns were acquired using a Panalytical X'Pert Pro diffractometer (Bragg-Brentano geometry, radiation Cu Kα, λ=0.154184 nm) and equipped with an ultrafast X'Celerator RTMS detector. The scans were performed in the 2_ range 10-90° with a resolution of 0.001°. The acquired scans were analysed using the X'Pert High Score Plus software. Making use of the ICDD PDF database, the phase identification was performed. Impurity traces were found in Cr_3C_2 and CrF_2: Cr_7C_3 and C, chromium oxyfluoride and chromium oxide, respectively.

1.2.3. microRaman

The samples were characterized by making use of a Renishaw inVia Raman Microscope (UK) equipped with Ar laser and blue line was used (λ = 488 nm, 2.54 eV).

Figure S3. microRaman spectra a λ = 488 nm of all 'as received' compounds of the electrodes of cell A. From the top: OLC & HOPG, Cr_3C_2 and CrF_2.

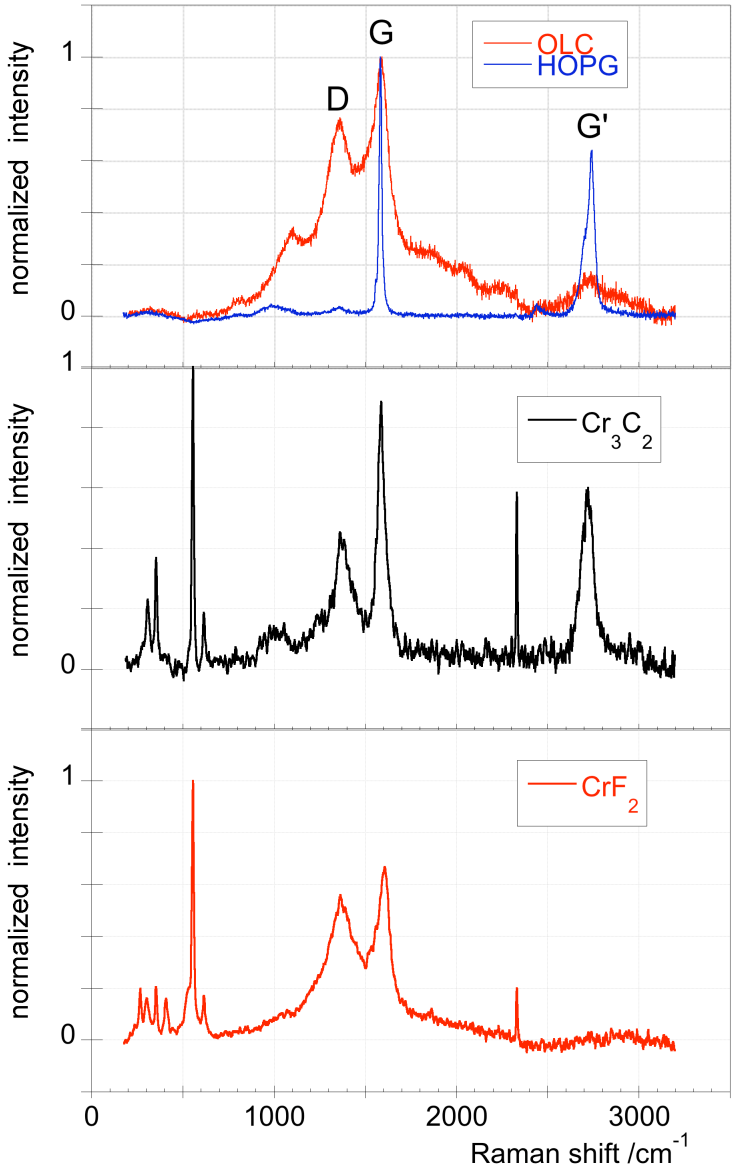

1.2.4. HR-TEM

TEM analyses were performed by a JEOL JEM 2200FS field emission transmission electron microscope operating at 200 kV (resolution: 0.19 nm) and Ω type energy filter. Samples for imaging were prepared by ultrasonic dispersion of small amounts of powders in isopropanol and then putting a drop of the dispersion on holey carbon-coated copper grids.

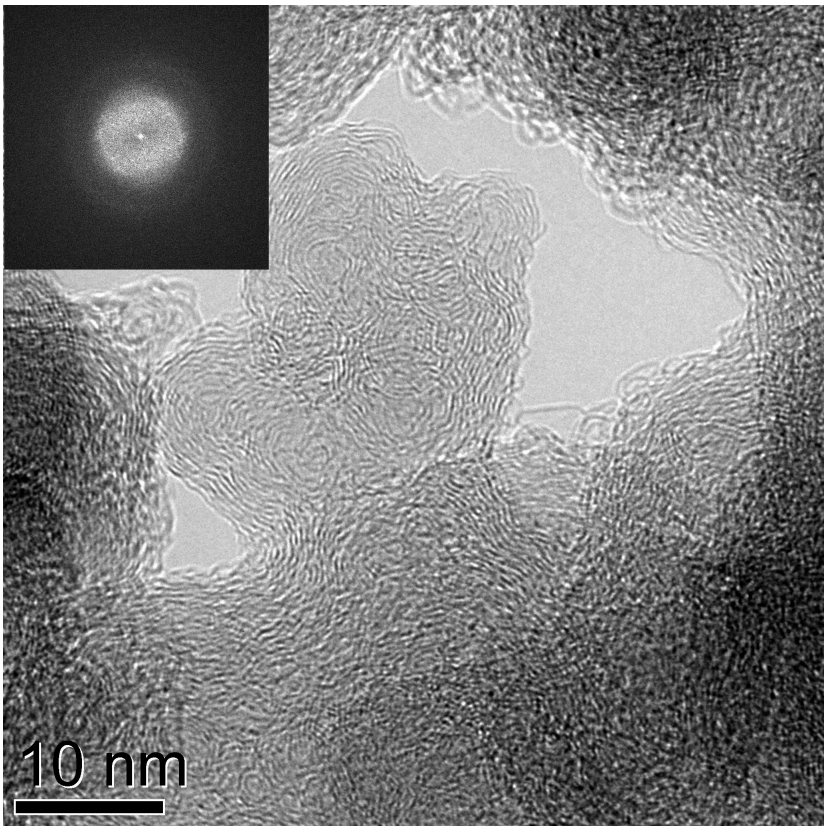

Figure S4. HR-TEM of the 'as received' OLC sample. The insetin the top left corner shows the FFT.

The inset shows the FFT. The rings expected for spacing parameters of graphite (c = 0.34 nm and a = 0.20 nm) are very weak indicating a low crystalline sample.

1.2.5. XPS

X-ray photoelectron spectroscopy was carried out by means of Thermo Scientific Theta Probe. The OLC sample, as well as the reference samples, was examined by depositing an isopropanol suspension directly onto a gold foil. The sample was then left to dry for several hours in the load lock chamber. It was analysed before and after Ar^+ etching in order to obtain a C1s signal free of contamination carbon. C1*s,* O1*s,* valence band and survey spectra of the carbon were measured in the standard emission geometry using a monochromatic Al Kα radiation photon energy 1486.6 eV. The high-resolution spectra were acquired setting two different pass energies (50 eV and 100 eV), while the survey spectra were recorded using pass energy of 200 eV. The energy resolution was determined from the Gaussian width of the C1*s* line of PET and it was found in these experimental conditions equal to 0.8 eV at pass energy of 50 eV. All measurements were carried out at the total pressure of 10^{-7} Pa. The spectra were processed using CASAXPS software (v2.3.15): curve fitting was performed after Shirley background subtraction. The

spectra of pure graphite were also collected using the same analysis conditions and the curve fitting parameters, i.e., the full width at half maximum of the peak height (fwhm), the G/L ratio and tail function (T) were constrained to the values acquired on HOPG and diamond. The C1*s* photoemission spectra of sp^2 bound carbon were fitted using a Gaussian component that accounts for the instrumental energy resolution together with any chemical disorder, combined with a Lorentzian width that accounts for the finite core hole lifetime associated with the photoionization process. Quantitative analysis was calculated using Scofield's photoionization cross-sections corrected for the asymmetry factor, intensity energy response function and inelastic mean free-path calculated using NIST approach [1].

Only carbon and oxygen were detected on the surface of OLC samples. The comparisons of C1s peak are reported in Figure S5 and in the table S1.

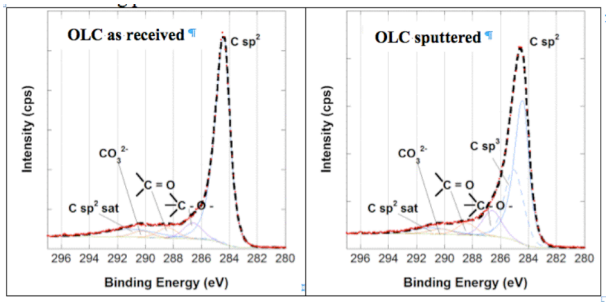

Figure S5. Comparison of XPS C1s spectra of OLC samples 'as received' (left side) and after sputtering (right side) .

Table S1. Binding energy values (eV), full width at half-maximum of the peak height. line-shape of the C1s signals and relative weight of the signals in the OLC sample before and after Ar^+ sputtering.

	C1s (1) sp^2	**C1s(2)** sp^3	**C1s(3)** C-O	**C1s(4)** C=O	**C1s (5)** CO_3^{2-}
OLC	284.4 eV (0.82) G/L(85)T(1.5) 84%	285.0 (1.65) G/L (30) 1%	286.6 eV (1.65) G/L (30) 7%	288.4 eV (1.65) G/L (30) 5%	290.2 eV (1.65) G/L (30) 3%
OLC sputtered	284.4 eV (0.82) GL(85)T(1.5) 55%	285.0 (1.65) GL (30) 28%	286.6 eV (1.65) GL (30) 10%	288.4 eV (1.65) GL (30) 5 %	290.2 eV (1.65) GL (30) 2%

As a consequence of Ar^+ sputtering a change in the shape of C1s is observed with an increase in the component at 285. 0 eV, that can be assigned to sp^3 carbon. The intensity of the component at 285.0 eV increases with sputtering time.

1.3. Preparation of electrodes and cell assembly

1.3.1. Electrodes

The electrodes were prepared in a glove box filled with inert and dry atmosphere according to the criterion of establishing the polyphasic coexistence through a close contact among the powder particles. Each powder mixture was prepared by mixing HOPG and OLC with CrF_2 and Cr_3C_2 in weight ratios 1:1:1 and 1:10:10 respectively. Each mixture was ball milled at 50 rpm overnight in a sintered alumina jar with sintered alumina spheres in order to ensure a truly intimate mixing of the phases. Possible modifications to the reactants were checked by XRD. Following the well-established standard procedure, the fine powder mixture was dispersed in acetone and, after evaporation of the solvent, pressed in a stainless steel mould at 0.6 GPa for obtaining cylinders 6 mm diameter x 3 to 5 mm height. The surfaces of electrodes were gently polished in such a way as to be flat and in perfect contact with the electrolyte surfaces.

1.3.2. Cell assembly

The cell holder containing the electrodes, electrolyte and Pt lead wires is machined from a workable alumina rod (Aremco, USA). Two small holes (1 mm dia.) serve as an outlet for the Mo wires and cell out gassing. All the components of the cell were assembled as a sandwich in which the electrolyte is in the middle. The electrolyte is a polished disk of CaF_2 monocrystal (MolTech GmbH, Germany) (111) oriented, 2 mm thick and 8 mm diameter. The total length of the cells was never greater than 12 mm. Molybdenum wires up to the feedthroughs of the furnace flange realized the electrical leads.

1.4. Experimental apparatus for the *emf* measurements

The *emf* measurements were carried out in a high-vacuum vertical furnace made of a W mesh resistor from Oxy-Gon Industries Inc., USA. An inconel spring-loaded latticework was utilized for positioning the holder of the electrochemical cell in the isothermal zone of the furnace. The vertical force applied to the cell is maintained at a preset value by a feedback motion device in such a way as to compensate size changes due to the temperature variations. In this way the contact pressure at the electrode/electrolyte interface is independent from temperature. Throughout the experiment the average hydrostatic pressure applied to cell was 12±3 kPa. The temperature was measured by two S-type (Pt/Pt-Rh 10%) thermocouples, which were calibrated against pure Au melting point. Before starting the *emf* measurements, the system was carefully flushed with Ar (O_2 < 1 ppm, H_2O < 1 ppm) and then outgassed by following a standard procedure, which does not allow any temperature increase of the cell if the pressure inside the furnace is greater than $1x10^{-6}$ mbar. The total pressure during the experiment is maintained below $1x10^{-7}$ mbar. A high impedance differential preamplifier (10^{15} ohm, typical bias current 40 fA) connected to one of the analog input channels of a data logger was used for the *emf* measurements.

1.5. Procedure adopted for the *emf* measurements and their data acquisition

The total accuracy, ε, in reading the *emf* was less than 50 μV. A data logger connected to a personal computer operating on a LabView© based program read the furnace and cell temperatures, pressure, *emf* as well as other signals. The stability of the temperature of the furnace at the set temperature was always within 1 K. The temperature changes throughout the experiments were performed by programmed ramps with a slope of ±3 K min^{-1}.

Each thermal cycle on the same cell was in general constituted of about 50 isotherms and each isotherm of 3 hours length was constituted by 150 point acquired. Data in Fig. 1 in the text

refer to 4 cycles (about 700 hours) on one out of five cells tested. The thermal cycle is programmed to scan the temperature interval up and down. A LabView© based software performs the off-line elaboration of data files by separating each isotherm and looking for the requirement of the *emf* stationary. This requirement for each isotherm is based on the convergence of the quantity calculated on every *i*-10 points. is the average of the *emf* values and its standard deviation. If the ratio converges to a value, which is within 10ε, the last is attributed to that isotherm with error bar equal to ± . The isotherm is discarded if this condition is not fulfilled. The temperature attributed to the accepted *emf* value is where and are respectively the average temperature and the related standard deviation on the whole isotherm.

1.6. Analysis of electrodes before and after experiment

1.6.1. XRD

The intensity full-scale range of the XRD pattern of the electrode with HOPG "before" (bottom-right panel) was reduced of one order of magnitude to make visible the features of Cr_3C_2 and CrF_2 with respect to the high intensity of the main peak of HOPG. Due to improved crystallization of CrF_2 with respect HOPG, the XRD pattern of the same electrode "after" can be shown (up-right panel) with its own full-scale range.

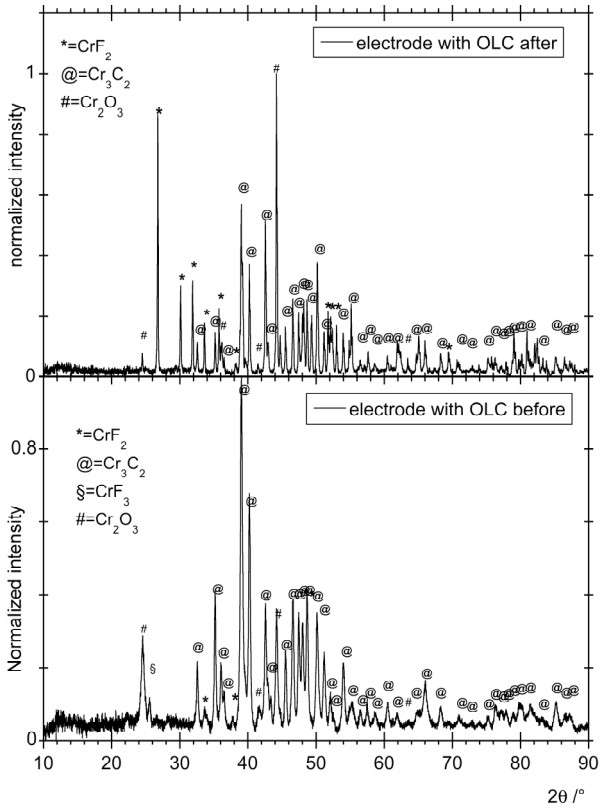

Figure S6. XRD comparison of the electrode powder mixtures containing OLC before and after an experiment. Due to the amorphous nature of OLC and their low content in the mixture, no features of them were detected. No evidence of new and/or disappeared phases was found.

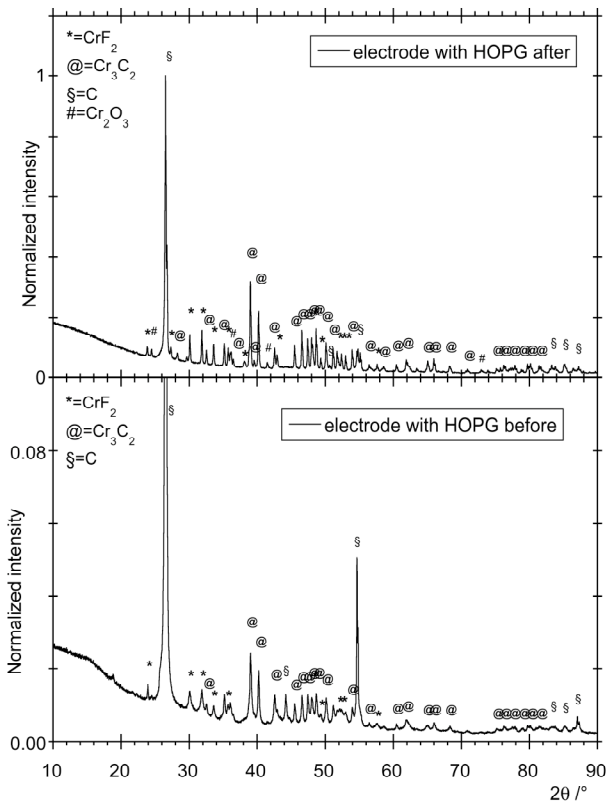

Figure S7. XRD comparison of the electrode powder mixtures containing HOPG before and after an experiment. The features of HOPG carbon were clearly detected in both cases. No evidence of new and/or disappeared phases was found.

1.6.2. microRaman spectroscopy (mR)

mR spectroscopy confirms further that no other chemical species were formed during the experiment because the spectra of both the electrodes did not change with exception of some differences in the intensity that are meaningless.

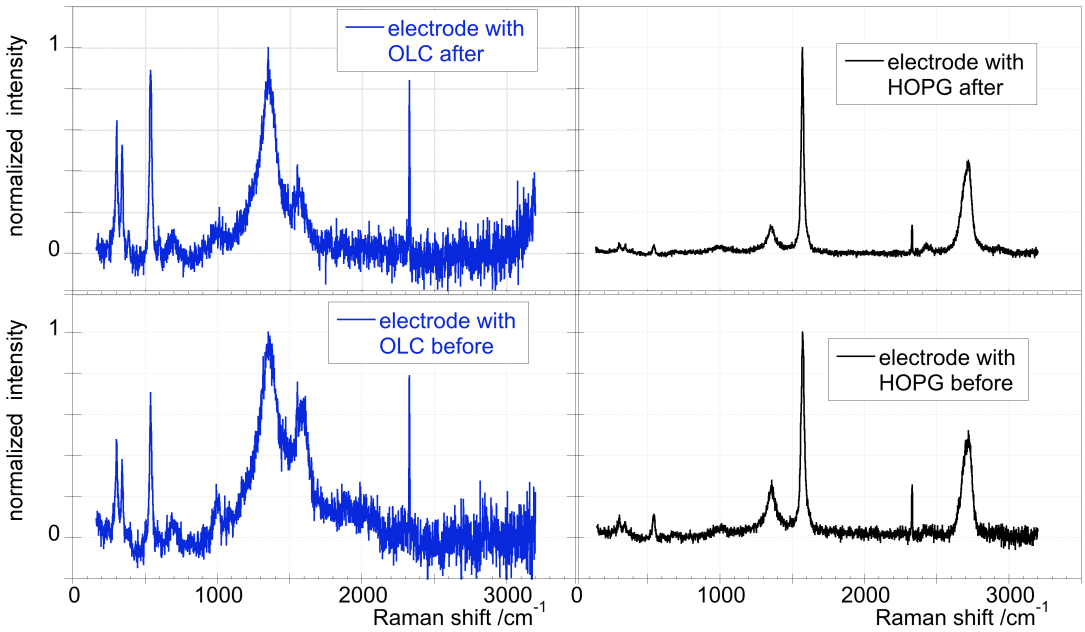

Figure S8. Comparison of the microRaman spectra of the electrode powder mixtures containing OLC (left side) and HOPG (right side) before and after an experiment. No evidence of changes was found.

1.6.3. EELS

This technique, as well as the XPS below, was utilized to determine the sp^2/sp^3 ratio in OLC by utilizing diamond and HOPG powder as standards for full sp^3 and sp^2, respectively. The carbon-K ionization edge (onset at 284 eV) were collected on a JEOL JEM-2200FS only on OLC hanging out in the grid holes, to avoid interferences from the carbon support film of the grids or from other parts of the samples. The acquisition of spectra was in "magic collection angle β" mode [2] with $\beta \cong 1.5$ mrad for carbon at 200 kV. The convergence angle $\alpha < \beta$ ensures that the effect due to the sample orientation gives a negligible error, which was found lower than the statistical one as verified on reference graphite. The samples were grinded and dispersed in isopropanol, and then deposited on holey carbon grids. The measurements have been carried out in many different regions of the samples to improve the statistics. Panel A of the figure below shows the EELS spectrum of the "as received" OLC sample (blue line) compared with OLC in the electrode after the experiment, the reference HOPG (black line) and amorphous carbon (green line). Panel B shows how the sp^2/sp^3 ratio was determined. This was done by the curve deconvolution [3] and Gaussian fit of the main σ* peak in the region 291-293 eV (green line). The π* contribution (red line) was obtained by subtraction of σ* peak from the total curve in the interval 280-292 eV. The sp^2/sp^3 ratio was evaluated by the ratios between the π* peak area of OLC samples as well as amorphous carbon and π* peak area of reference graphite. The sp^2 carbon coordination

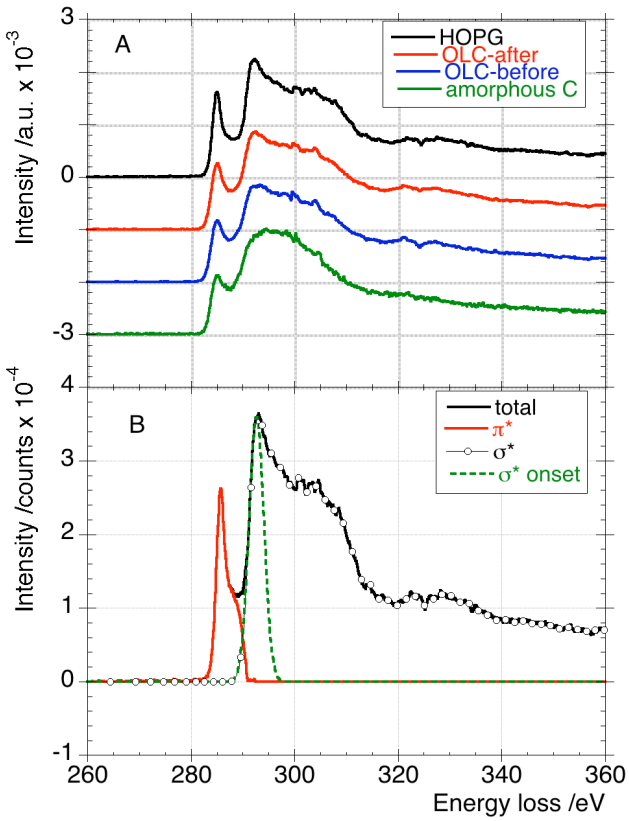

values were found 82±3 %, 86±3 % and 69±8 % for OLC before and after and amorphous carbon, respectively. The result points to a graphitization of OLC towards multi-shell ordered structures in the process, as confirmed by clearer reflections in the FFT of the HRTEM images after the experiment, corresponding to the expected graphite reflections. The planes are bended to form the spherical structures seen in the HRTEM images of Fig. 8B in the text.

Figure S9.
A. EELS spectra of OLC before and after an experiment compared with two references for sp^2 content HOPG and amorphous carbon.
B. Evaluation of the sp^2/sp^3 ratio in the OLC samples.

1.7. **Derivation of eq 18**

The relationship between σ and γ reads,

$$\gamma = \sigma + A\frac{d_s\sigma}{d_sA} \tag{1}$$

where A denotes the area of the surface and the subscript s reminds us that the variation is performed by stretching. Let us consider a one–component nano particle of radius r in equilibrium with its vapour at constant temperature and volume. At equilibrium $dF = 0$, with F being the Helmholtz free energy:

$$dF = (\mu_B - \mu_V)dN + \sigma\frac{\partial A}{\partial N}dN + \frac{\partial F_r}{\partial N}dN = 0 \tag{2}$$

that is

$$\mu_V = \mu_B + \sigma\frac{\partial A}{\partial N} + \frac{\partial F_r}{\partial N} \tag{3}$$

In this equation μ_B and μ_V are the chemical potentials of the components in the Gibbs model system ($r \to \infty$) and in the vapour, respectively; $F_r < 0$ is the relaxation energy that depends on deformation of both surface and bulk of the particle. Accordingly, the surface energy (σ) refers to unrelaxed surface, i.e., to a particle of infinite radius. Moreover, the Laplace equation gives the pressure difference between the two phases (particle-vapour) as,

$$P_i - P_{ex} = \frac{2\gamma}{r} \tag{4}$$

where P_i is the pressure in the particle and P_{ex} the external pressure. It is evident from eq 4 that the particle is in a state of compression for $\gamma > 0$. Consequently, the volume change of the particle (on going from P_{ex} to P_i) owing to the surface tension can be computed by means of the compressibility, κ, as $\frac{\Delta V}{V} = -\kappa \left(P_i - P_{ex}\right) = -\kappa \frac{2\gamma}{r}$, with V being the particle volume.

Let us now compute the relaxation energy term, F_r. To this purpose, it is considered a closed system made up of particle and vapour phases at constant total volume. One estimates the energy change for the relaxation of the surface through stretching which entails the pressure difference given by eq 4. The whole energy change is given by the sum of the following contributions: $F_r = \Delta F_V + \Delta F_1 + \Delta F_2$ where ΔF_V is the term linked to the vapour, ΔF_1 is the energy term due to the "volume" strain of the particle and ΔF_2 is the surface tension contribution. For uniform compression the $\Delta F_1 > 0$ term is given by $\Delta F_1 = \frac{1}{2}\kappa V\left(P_i^2 - P_{ex}^2\right) = \frac{\gamma\kappa V}{r}\left(\frac{2\gamma}{r} + 2P_{ex}\right)$, where eq 4 was employed. The change of the energy of the vapour is given by $-P_{ex}\Delta V_V = P_{ex}\Delta V = -P_{ex}V\kappa\frac{2\gamma}{r}$. Furthermore, the energy gained by the system due to the work done by the surface tension reads: $\Delta F_2 = \gamma A\frac{\Delta A}{A} = \frac{2}{3}\gamma A\frac{\Delta V}{V} = -\frac{4}{3}A\kappa\frac{\gamma^2}{r}$. The relaxation energy is computed eventually as ($A = 4\pi r^2$):

$$F_r = \frac{\gamma\kappa V}{r}\left(\frac{2\gamma}{r} + 2P_{ex}\right) - P_{ex}V\kappa\frac{2\gamma}{r} - \frac{16}{3}\pi r\kappa\gamma^2 = \frac{8}{3}\pi r\kappa\gamma^2 - \frac{16}{3}\pi r\kappa\gamma^2 = -\frac{8}{3}\pi r\kappa\gamma^2 \qquad (5)$$

It is instructive to verify that eq 5 is in fact the energy change linked to the generation of the excess hydrostatic pressure of eq 4. The relation holds:

$$F_r = \int_{\Delta P=0}^{\Delta P=2\gamma/r} \Delta P\,dV = -\kappa V\int_0^{2\gamma/r} \Delta P\,d\Delta P = -\frac{8}{3}\pi r\kappa\gamma^2\,, \qquad (6)$$

which coincides with eq 5. By inserting the F_r expression in eq 3 and considering that for the spherical shape $\frac{\partial A}{\partial N} = \frac{\partial A}{\partial V}\frac{\partial V}{\partial N} = \frac{2V}{r}$ and $\frac{\partial F_r}{\partial N} = \frac{V}{4\pi r^2}\frac{\partial F_r}{\partial r}$, V being the molar volume of the solid, one gets

$$\mu_V = \mu_B + \sigma\frac{2V}{r} - \frac{2V}{3r^2}\kappa\gamma^2 \qquad (7)$$

Therefore, the chemical potential difference between the components in the particle and in the bulk phase is equal to [4]

$$\Delta\mu_s = \frac{2V}{r}\left(\sigma - \frac{\kappa\gamma^2}{3r}\right) \qquad (8)$$

where the subscript *s* emphasises that this contribution is entirely due to the interface.

1.8. **Derivation of eq 22**

The integration of equation $\left(\frac{\partial U}{\partial V}\right)_T = T\left(\frac{\alpha}{\kappa}\right) - P$ gives at constant temperature:

$$\Delta U = \left(U - U_0\right)_T = T\int_{V_0}^{V}\frac{\alpha}{\kappa}dV - \int_{V_0}^{V}P\,dV = T\frac{\alpha}{\kappa}\left(V - V_0\right) - \int_{V_0}^{V}P\,dV \quad . \tag{9}$$

Due to the definition of the isothermal compressibility κ, the volume V can be written as $V = V_0 e^{-\kappa P}$ and the term $-\int_{V_0}^{V}P\,dV$ becomes:

$$-\int_{V_0}^{V}P\,dV = V_0\kappa\int_{0}^{P}Pe^{-\kappa P}\,dP = \frac{V_0}{\kappa}\left[1 - \left(1+\kappa P\right)e^{-\kappa P}\right] \tag{10}$$

being $\int xe^{ax}dx = \frac{e^{ax}}{a^2}\left(ax-1\right)$. By substituting eq 10 in eq 9, eq 22

$$\Delta U = \left(U - U_0\right)_T = \frac{V_0}{\kappa}\left\{\left[1 - \left(1+\kappa P\right)e^{-\kappa P}\right] + \alpha T\left(e^{-\kappa P} - 1\right)\right\}$$

is obtained.

1. Gries, WH (1996) A universal predictive equation for the inelastic mean free path lengths of x-ray photoelectrons and auger electrons. Surf. Interface Anal. 24: 38–50.
2. Egerton RF (1996) Electron energy-loss spectroscopy in the electron microscope. 2nd Ed., Plenum Press, New York.
3. Verbeeck J, Bertoni G (2009) Deconvolution of core electron energy loss spectra Ultramicroscopy 109: 1343-1352.
4. Shuttleworth R (1950) The Surface Tension of Solids. Proc Phys Soc (London) A 63: 444-457.